University of Johannesburg
Department of Physics

Characterization of Incomplete Fusion Reactions with DIAMANT and AFRODITE

A dissertation submitted in fulfillment

of the requirements for the degree of Masters in Philosophy(M. Phil.)- Energy Studies

by
Bongani Goodman Maqabuka

Supervisor: **Dr. Simon M. Mullins**

iThemba LABS

Johannesburg

Co-supervisor: **Prof. Simon H. Connell**

Department of Physics

University of Johannesburg

2014

Candidate's Declaration

I declare that this dissertation is my own, unaided work. It is being submitted in fulfilment of the requirements for the degree of Master of Philosophy at the University of Johannesburg, Johannesburg. It has not been submitted before for any degree or examination at any other University.

———————————————

Bongani Goodman Maqabuka

——————————— day of ——————————— 2014

i

Dedication

*This work is dedicated to my grandparents **Kay Maliwa, Mangcoya** and **Nozipo Maqabuka** (R.I.P.).*

Acknowledgements

Abstract:

This project concerns the study of nuclear reaction mechanisms, specifically, the incomplete fusion mechanism. The nuclear reaction ^{7}Li + ^{176}Yb at 50 MeV was therefore carried out using the AFRODITE and DIAMANT facility of iThemba LABS.

A ^{7}Li nuclide is considered suitable for the breakup fusion (incomplete fusion) reaction because of its well developed cluster structure of an α-particle and *triton* which are weakly bound in this nucleus. One of the breakup fragments may be captured by the target while the other escapes at the beam velocity. Light charged-particles (alpha, tritons, deuterons and protons) were detected with the DIAMANT (CsI) array in co-incidence with gamma-rays detected by the AFRODITE (HPGe) spectrometer. The light particle detection in co-incidence with gamma detection was an important innovation that allowed exclusivity in the reconstruction of the mechanism by which specific residues were produced.

Off-line data processing was used to produce charged-particle-gated gamma-gamma coincidence matrices which were analysed with the RADWARE software package. The level scheme exclusive to a particular channel for the production of the ^{178}Hf was extracted. The relative cross-section for the various reaction channels could also therefore be extracted. In particular, the intensity ratios of gamma transitions as function of spin for proton to triton-gated matrices populating the ^{178}Hf isotope were extracted. Insights could be developed into the incomplete fusion reaction mechanisms initiated by the breakup of the incident ^{7}Li projectile.

Contents

List of Figures

UNIVERSITY
OF
JOHANNESBURG

List of Tables

Chapter 1

INTRODUCTION

The influence of projectile breakup on fusion and other reaction processes is currently a hot topic for both theoretical and experimental nuclear physicists who seek to understand the incomplete fusion reaction dynamics in heavy ion interactions. Fusion between two nuclei occurs when the projectile overcomes the *barrier* resulting from the sum of the long-range repulsive Coulomb potential and the short-range attractive nuclear potential. However, the situation is more complicated when dealing with weakly bound nuclei, since they may break up before reaching the target nucleus. Under such circumstances, two different fusion processes are possible: (i) **complete fusion** (CF), defined in principle as the capture of all the mass of the projectile by the target, and (ii) **incomplete fusion** (ICF), which happens when one of the breakup fragments is captured by the target. Incomplete fusion leads to an anisotropy in the angular distribution of the emitted particles. An account on the details of the two processes is given in Chapter 2. Studies done by Dracoulis *et al.* [1] suggest that the presence of incomplete fusion, enhancing the anisotropy in the angular distribution of emitted particles, produces different intensities of γ-transitions when in coincidence with particles detected at forward or middle and backward angles (i.e. yield ratios) for the isotopes produced in the heavy-ion reaction.

In this work we investigate the ICF mechanism following the breakup of ^{7}Li projectiles incident on a target of ^{176}Yb by looking at the ^{178}Hf isotope populated through the (^{6}He, 4n) and (^{4}He, 2n) exit channels. The experiment was performed as part of ATOMKI, Hungary-iThemba LABS, Stellenbosch collaboration. The purpose of this collaboration is to obtain comprehensive information on the dynamics of reactions induced by weakly bound light charged particle nuclei such as ^{7}Li, ^{9}Be, ^{11}B, etc., establishing a comprehen-

sive phenomenological description of such reactions. The ^{7}Li beam was generated as a collaborative effort between ion source experts at iThemba LABS and the Flerov Laboratory for Nuclear Reactions (FLNR) of the Joint Institute for Nuclear Reactions (JINR), Dubna-Russia.

A whole host of nuclei in the mass region 180 were populated in this experiment. These nuclei are located in a region of deformation. This region is characterised by collective rotational behaviour which coexists with intrinsic quasiparticle modes of excitation as a means with which to form the yrast line. These quasiparticle states have large K values which arise as a result of the large angular momentum projections (Ω) of the single-particle orbitals on the nuclear symmetry z-axis. Electromagnetic transitions of multipolarity λ between high K states are in principle forbidden if ΔK is greater than the multipolarity, λ of the photon [2]. This makes the excited quasiparticle states to be metastable (isomeric) in character. Bands built on these metastable states are decoupled from the level scheme below due to the isomeric nature (i.e. having long lifetimes) of these bandhead states. This makes it difficult, to assign these bands to a particular isomer, and indeed to the nucleus itself. However, studies carried out by Mullins et $al.$ [3, 4], show that there is a distinct correlation between the relative gamma-ray intensities of the product nuclei when selected by alpha/triton-particles detected at forward or middle/backward angles. We explore these correlations in gamma-ray intensity ratios for the various bands of the ^{178}Hf nucleus populated through forward gated proton or triton-particles, i.e. the (^{6}He, 4n) and (^{4}He, 2n) exit channels.

Following this introduction, Chapter 2 describes the methods and some of the technical details of the experiment. Theoretical models which lay out the theoretical framework used in the description of the ^{178}Hf nuclear structure are described in Chapter 3. An analysis of the data and discussion of the results is done in Chapters 4 and 5.

Chapter 2

EXPERIMENTAL METHODS AND DETAILS

2.1 Fusion Reactions

Atomic nuclei present many challenges to detailed experimental examination. One of those challenges is mainly due to its size, of the order of 10^{-15}m in diameter. Heavy-ion fusion followed by nucleon evaporation has become one of the main techniques of producing nuclei at high excitation energy and spin in order to study the properties of nuclear excitations using gamma-ray spectroscopy.

2.1.1 Fusion with Weakly Bound Projectile Nuclei

The nucleus ^{7}Li, the beam that was used in the experiment for this work, is bound against decay into its two constituents (the α and the *triton*) by only 2.47 MeV. This means that it is comparatively loosely bound, although it is a stable nucleus. The α plus *triton* cluster structure of ^{7}Li should result in a breakup yield of these fragments. There are many processes that can possibly take place (as this is a random process) during the reaction with such weakly bound projectiles:

- The whole of the projectile fuses with the target, a process called *direct complete fusion* (DCF) i.e. $^7\text{Li} + ^{176}\text{Yb} \longrightarrow ^{183}\text{Ta}^* \longrightarrow ^{(183-x)}\text{Ta} + xn$.

- In some instances prior to fusion, the projectile breaks up in the field of the target

nucleus and subsequently all the fragments fuse with the target to form a compound nucleus. This process is referred to as *sequential complete fusion* (SCF). The compound nucleus produced in both DCF and SCF is identical, experimentally it is not possible to distinguish between the two processes, hence they are referred to as *complete fusion* (CF).

- Following the breakup of the projectile in the target field, one of the fragments may be captured by the target nucleus leaving one flying past with the beam. This process whereby only one of the projectile fragments is absorbed by the target is called *incomplete fusion* (ICF) or a *massive transfer* reaction process [5, 6, 7] i.e.
$^7\text{Li}(\alpha + t) +^{176}\text{Yb} \longrightarrow ^{179}\text{Lu}^* \longrightarrow ^{(179-x)}\text{Lu} + \alpha + xn$ or
$^7\text{Li}(\alpha + t) +^{176}\text{Yb} \longrightarrow ^{180}\text{Hf}^* \longrightarrow ^{(180-x)}\text{Hf} + t + xn$.
Also possible is the breakup of the projectile, $^7\text{Li} \longrightarrow ^6\text{He} + p$ with the ^6He proceeding to fuse with the target i.e. $^7\text{Li}(^6\text{He} + p) +^{176}\text{Yb} \longrightarrow ^{182}\text{Hf}^* \longrightarrow ^{(182-x)}\text{Hf} + p + xn$.
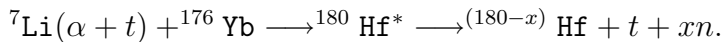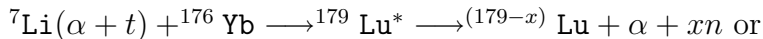
The two latter reaction processes leading to the population of ^{178}Hf isotope is the area of interest in this thesis. Typical fusion reactions would proceed as illustrated in Figure 2.1.

2.1.2 The Complete Fusion Reaction

Fusion is defined as an amalgamation of two nuclei to form a highly excited, compound nucleus, which decays by successive particle emission to produce heavy evaporation residues [8]. The heavy residual nucleus from which further particle emission is energetically not possible, decays to the ground state by emitting gamma-ray cascades. This happens when a beam of ionized nuclei of a specific isotope is accelerated onto a target placed in the target chamber. If the two nuclei collide with a sufficiently small *impact parameter*, as depicted in Figure 2.1 and large energy such that their mutual *Coulomb repulsion*, i.e. the Coulomb barrier is overcome, their nuclear potentials overlap to form a *single compound nucleus*. The density distributions of these nuclei start to penetrate each other, the kinetic energy of nucleons is dissipated in collisions between nucleons originating from different nuclei. The energy dissipation can be imagined as a result of a frictional force. This force, qualitatively reduces the radial motion and transforms the relative angular momentum into intrinsic angular momentum of the compound nucleus [10].

The Coulomb barrier energy V_{cb} (in MeV) can be determined by the following equation [11]
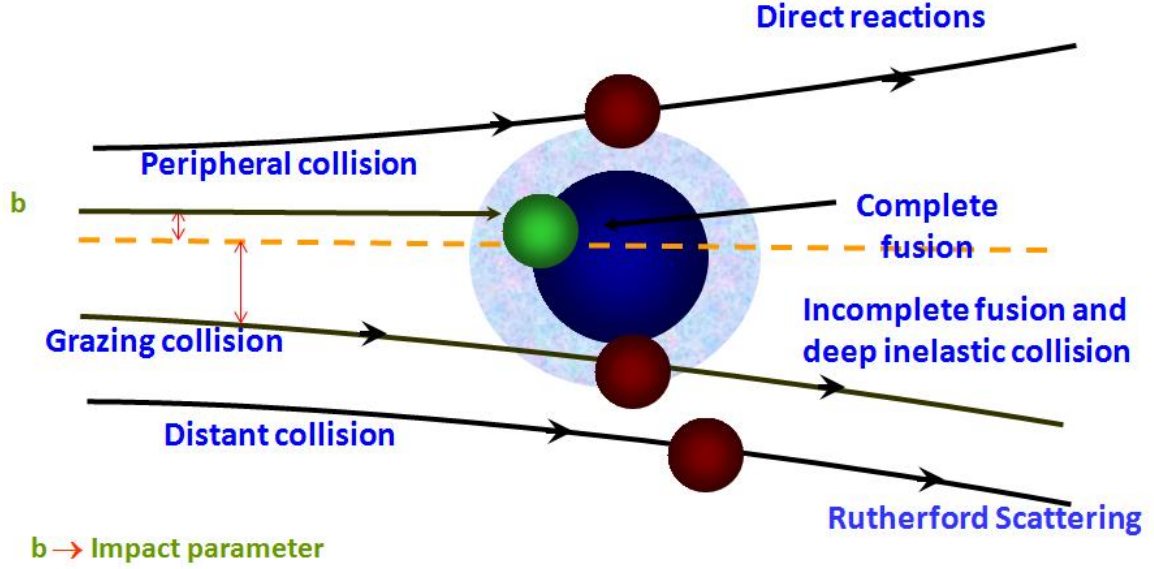
Figure 2.1: Heavy-ion collisions with a nucleus (the target) as a function of impact parameter [9].

$$V_{cb}(R) = \frac{1}{4\pi\varepsilon_0} \frac{Z_b Z_t e^2}{R}, \tag{2.1}$$

where Z_b and Z_t are the atomic number for the beam and target nuclei, respectively, ε_0 is the permittivity of free space, e is the charge of an electron. R (in fm) is the maximum nucleus-nucleus distance for which a reaction can take place and is given by the expression [12]

$$R = 1.36(A_b^{\frac{1}{3}} + A_t^{\frac{1}{3}}) + 0.5. \tag{2.2}$$

After collision the compound nucleus loses all the memory of the components involved in its formation process, with the kinetic energy of the particle or fragment of beam particle being randomly distributed between the nucleons in the compound system [13, 14]. The decay probability is dependent only on the total energy given to the system, not on the nature of the initial nuclei, whereas the angular momentum limit in a certain compound nucleus at a given excitation energy is dependent on the entrance channel.

The kinetic energy of the collision and relative momentum of the projectile and target are converted into excitation energy and angular momentum of the compound system. The

excitation energy of the compound system is given by [15]

$$E_x = \frac{M_t}{M_b + M_t} E_b + Q, \tag{2.3}$$

where M_t and M_b are the mass of the target and beam respectively, E_b is the beam energy, and Q is the energy (mass) difference between the reactants and the product which can be expressed as

$$Q = (M_b + M_t - M_{cn})c^2, \tag{2.4}$$

where M_{cn} is the mass of the compound nucleus. The fusion reaction process is a random process and, as such, the compound nucleus system can assume a wide range of angular momentum values. The central and/or near-central trajectories with $0 \leq \ell \leq \ell_{crit}$ values lead to complete fusion. Incomplete fusion, as will be discussed in next section, takes place over a narrower range of angular momentum compared to complete fusion. It is more favoured at peripheral (grazing) collisions of the impact parameter. The maximum amount of angular momentum which can be induced onto the compound nucleus system following a reaction is given by [11]

$$l_{max} = \sqrt{\frac{2\mu R^2}{\hbar^2}(E_{cm} - V_{cb})}, \tag{2.5}$$

where E_{cm} is the kinetic energy in the centre of mass of the system, i.e. the kinetic energy of the collision which is transferred to the compound system and μ is the reduced mass given by

$$\mu = \frac{M_b M_t}{M_b + M_t}. \tag{2.6}$$

At the stage of formation, the compound nucleus has a high excitation energy which must be dissipated in order to allow the system to reach its lowest energy state, the *ground state*. This is achieved at first through isotropic emission of neutrons, protons and α-particles in the centre-of-mass frame. The compound nucleus is also at risk of fissioning at any step of the compound-nucleus formation and decay process. The competition between fission, light-particle evaporation and γ-ray emission continues from the compound-nucleus formation down to the ground state of evaporation residue. As a result, this competition has to be taken into account during cross-section determination.

Protons and α-particles are charged, they are inhibited from passing through the Coulomb barrier allowing mainly neutrons to pass through. Each neutron carries away 1-2 MeV of kinetic energy in addition to the binding energy of about 8 MeV, but only takes away 1-2$\hbar$ of angular momentum. This leaves the residual nucleus with a high angular momentum relative to the energy it possesses. The compound nucleus becomes the final
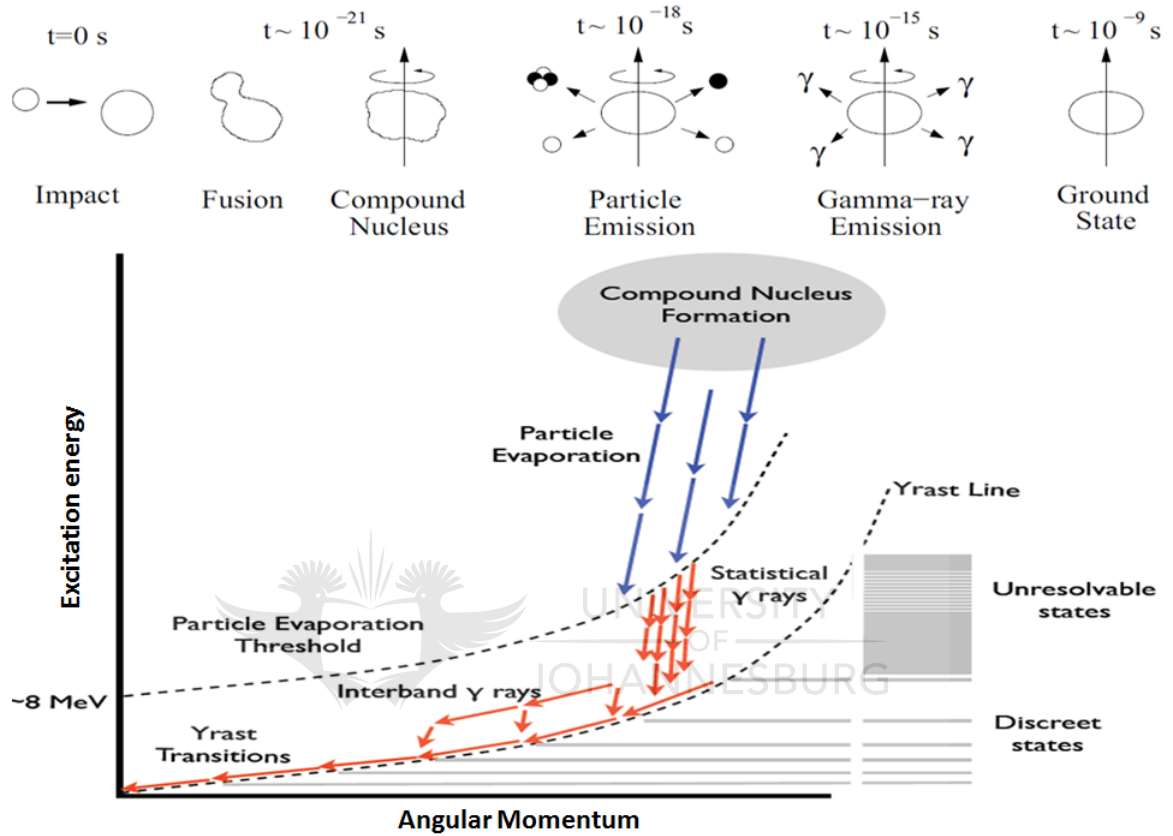
Figure 2.2: A plot of the excitation energy as a function of angular momentum showing the various stages of the compound nucleus formation and as it de-excites from the excited state, first by emission of charged particles and finally statistical gamma-rays. The average time scale of each step in the compound-nucleus formation is shown [13, 11].

residual isotope once it has finished emitting further particles. At this stage the number of nucleons in the residual nucleus has become fixed. The compound nucleus has reached an energy below the minimum particle separation energy required to further release nucleons. At this point the so-called statistical gamma-ray transitions (typically E1) take place approximately 10^{-15}s after impact and are followed by a cascade of gamma-ray transitions (typically E2 transition for quadrupole deformed nuclei) approximately 10^{-12}s after impact. These gamma-rays take away the remaining angular momentum and excitation energy of the compound nucleus system. The compound nucleus is at first, in a "chaotic" state with a high density of levels, a continuum of unresolvable gamma-rays. With loss of energy the nature of states changes from continuum to discrete. The final stage of the fusion-evaporation reaction is when the nucleus approaches the *yrast* line i.e. the sequence of states, with the lowest energy for a given spin. At this stage discrete cascades can be observed. The fusion-evaporation process with a typical time scale is illustrated in Figure 2.2. With the emission of many neutrons during fusion reactions, neutron-deficient nuclei tend to be populated.

2.1.3   The Incomplete Fusion Reaction

In an incomplete fusion reaction you have the breakup of the projectile prior to fusion process, as opposed to complete fusion where the whole projectile fuses with the target nuclei thus transferring all its *linear momentum*. As a result the compound nucleus is formed with less than the full available momentum and mass/charge of the projectile. Part of it is taken away by the fractional emitted particle. Breakup products from the incomplete fusion reaction will be more forward focussed than the isotropic distribution characteristic of complete fusion.

For an example a ^{7}Li beam incident on a heavy target exhibits the products which can be interpreted as breakup of ^{7}Li into an α-particle and a *triton*. One of the fragments proceeds to fuse with the target. If the fragment that fuses with the target is an α-particle, the effective energy of the α-particle would be given by the expression

$$E_\alpha = \frac{4}{7}[E_b + E_s(^7\text{Li} - triton)]. \tag{2.7}$$

An incomplete fusion reaction is more enhanced within a narrow grazing range of impact parameter, i.e. at non-central trajectories as illustrated in Figure 2.1, just above the critical angular momentum ($\ell \geq \ell_{crit}$) for complete fusion. Where ℓ_{crit} for complete fusion

can be determined from the relation [16]

$$4\pi\gamma\frac{R_1 R_2}{R_1 + R_2} = \frac{Z_1 Z_2 e^2}{(R_1 + R_2)^2} + \frac{l_{cr}(l_{cr} + 1)\hbar^2}{\mu(R_1 + R_2)^2},$$ (2.8)

where γ denotes the coefficient of surface tension and is given by

$$\gamma = 0.95 \text{MeVfm}^{-2},$$ (2.9)

and the radii R_1 and R_2 may be computed from the relation

$$R_i = 1.128 A_i^{1/2}(1 - 0.786 A_i^{-2/3}) \text{fm},$$ (2.10)

with $i = 1, 2$.

2.2   Reaction Choice and Characteristics
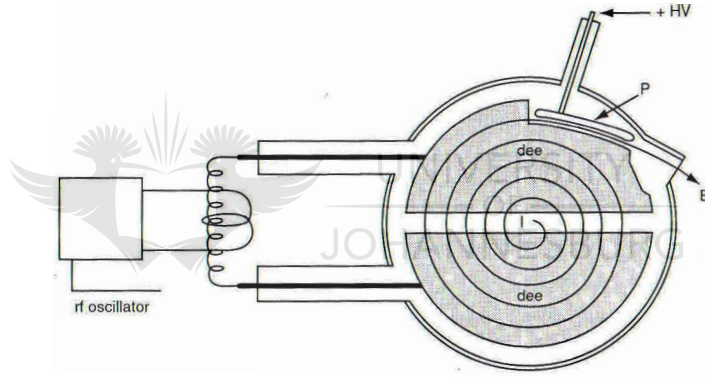
Figure 2.3: A schematic diagram of a cyclotron accelerator.

In this work a ^{7}Li heavy ion beam at 50 MeV was used to bombard ^{176}Yb target at the iThemba LABS cyclotron facility near Cape Town. A cyclotron uses multiple acceleration by a radio frequency electrical field, see Figure 2.3. The ions in a cyclotron are constrained by a magnetic field to move in a spiral path.

The ions are injected at the center of the magnet between two semicircular electrodes called *dees*. As the particle spirals outward it gets accelerated each time it crosses the gap between the dees. The time it takes a particle to complete an orbit is "isochronous", since the distance it travels increases at the same rate as its velocity, allowing it to stay in phase with the radio frequency.

In order to achieve good results for an experiment, target quality in a reaction is an important factor. The target material within the foils must be isotopically enriched to high purity levels, in excess of 95%, to reduce the effect of contaminants which may lead to unwanted reaction products. This entails having the right target thickness, a balance between achieving high statistics in an experiment and the best γ-ray energy resolution. With thicker targets the number of interactions between the beam and target is increased leading to added complexity in the analysis and uncertainties in the final results.

2.3 Interaction of Gamma Rays with Matter

The study of nuclear-radiation detection requires an understanding of the interaction of radiation with matter. Gamma-rays and X-rays are two forms of electromagnetic radiation differing only in their origins. One originating from the nucleus, the gamma-rays, and the other at an atomic level. The emission of gamma-rays is a mechanism by which the energy of the excited nucleus can be removed. Such excited states may result from the decay of radioisotopes, or they may result from induced nuclear transformations.

The gamma-rays accompanying a particular type of nuclear reaction are photons with energy E_p, given by the expression

$$E_p = h\nu = \frac{hc}{\lambda},$$ (2.11)

where
h = Planck's constant,
c = Speed of light,
ν and λ being the frequency and wavelength, respectively, which are associated with the wave nature of the radiation. Typical energies of gamma-rays range from a few keV to several MeV. The interaction of gamma-rays with matter is primarily through three mechanisms, namely, the *Photoelectric effect*, *Compton scattering*, and *Pair production*.

2.3.1 Photoelectric Absorption

In the photoelectric effect a photon of energy $h\nu$ interacts with the atom as a whole. Its energy is transferred to an electron, usually in the inner-most shell of the atom. The electron is ejected from the atom with a kinetic energy E_{kin} given by

$$E_{kin} = h\nu - E_b,$$ (2.12)
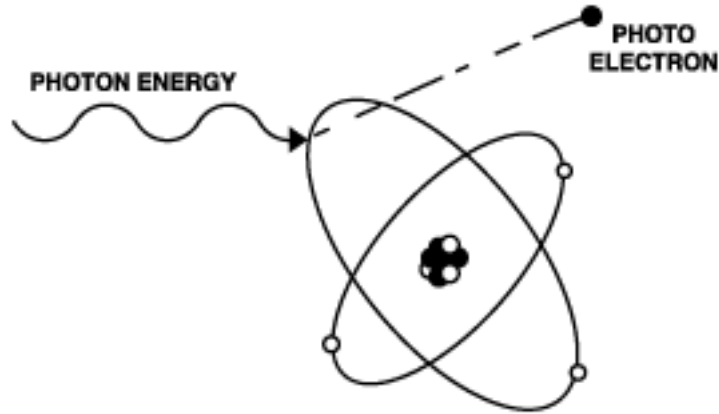
Figure 2.4: Schematic diagram of photoelectric absorption.

where E_b is the binding energy of the orbital electron. In addition to the photo-electron, the interaction also creates an ionized absorber atom with a vacancy in one of its bound shells. That vacancy gets filled by electrons in the upper shell of the atom or the capture of a free electron from the medium. As a result, one or more characteristic X-rays with total energy E_b are emitted. The photoelectric effect is the predominant mode of interaction for gamma-rays of relatively low energy (less than 200 keV) and its cross-section falls rapidly with increasing photon energy.

2.3.2 Compton Scattering

In Compton scattering the primary photon may interact with any of the orbital electrons in the absorbing material. The incoming gamma-ray photon is deflected through an angle θ with respect to its original direction. The photon transfers a portion of its energy to the electron, which is called the *recoil electron*. The energy transferred to the electron can vary from zero to a large fraction of the gamma-ray energy depending on the angle of deflection/scattering of the photon. Using the equations for the conservation of energy and momentum one can derive the expression that relates energy transfer and the scattering angle. For energy conservation, we must have

$$E_\nu + m_o c^2 = E_\nu' + E_e, \qquad (2.13)$$

11
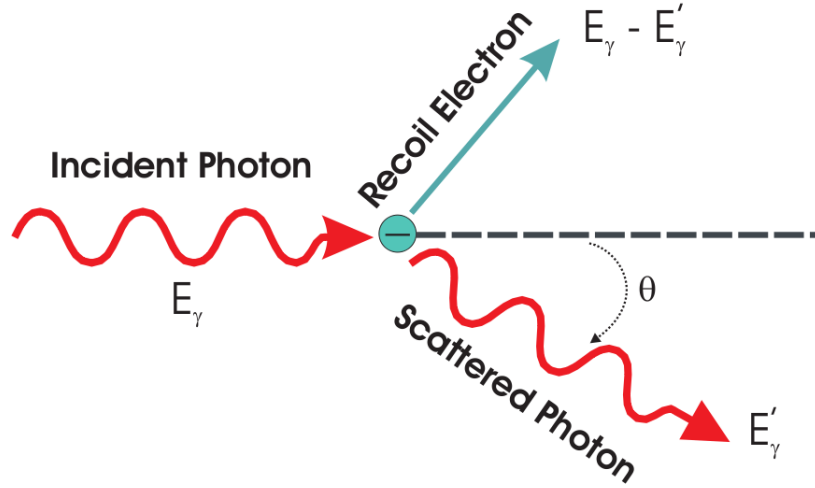
Figure 2.5: Schematic diagram of Compton scattering.

and for the conservation of momentum, using the cosine formula, we have

$$\mathrm{p}_e{}^2 = \frac{{E'_\gamma}^2}{c^2} + \frac{{E_\gamma}^2}{c^2} - \frac{2E_\gamma E'_\gamma}{c^2}\cos\theta, \tag{2.14}$$

but

$$E_e^2 = \mathrm{p}_e^2 c^2 + m_o^2 c^4. \tag{2.15}$$

The solution of these equations gives us

$$\frac{1}{E'_\gamma} - \frac{1}{E_\gamma} = \frac{1}{m_o c^2}(1 - \cos\theta), \tag{2.16}$$

where $m_o c^2$ is the rest-mass energy of the electron (0.511 MeV).The relation between the scattering angles of the photon θ and the electron ϕ is given by the following expression

$$\cot\frac{\theta}{2} = \left(1 + \frac{h}{\lambda m_o c}\right)\tan\phi. \tag{2.17}$$

The probability of Compton scattering per atom of the absorber depends on the number of electrons available as scattering targets and as such increases linearly with Z. The energy range for Compton scattering is about (200 - 5000 keV).

2.3.3 Pair Production

Pair production takes place when the gamma-ray exceeds twice the rest-mass energy of an electron (1.022 MeV). The primary photon disappears as it passes near a nucleus, and its

12
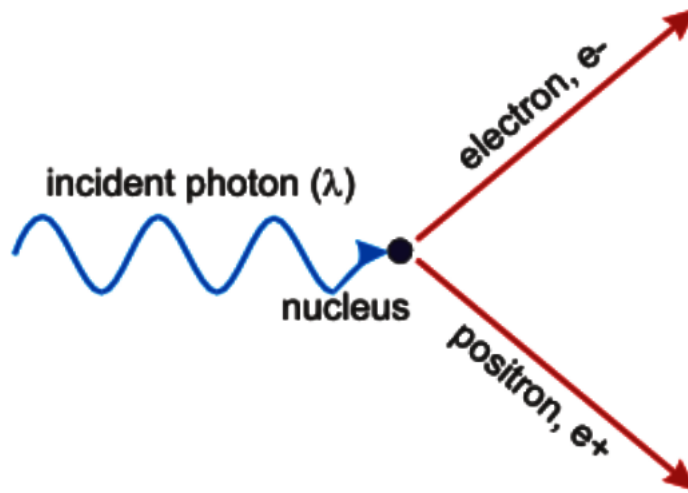
Figure 2.6: Schematic diagram of the pair production process.

energy goes into rest-mass energy and the kinetic energy of the positron e^+ and electron e^- pair which is produced [17]. This transformation of energy into mass must take place near a particle, such as a nucleus, in order for momentum to be conserved. The kinetic energy of the pair can be expressed as follows

$$
\begin{aligned}
E_{kin} &= E_\nu - 2m_o c^2 \\
&= E_\nu - 1.022 \text{MeV}.
\end{aligned}
\tag{2.18}
$$

The probability of this interaction remains very low until the gamma-ray energy approaches several MeV's.

2.4 Nuclear Radiation Detection

Most of the major discoveries in nuclear physics during the last four decades can be associated with detector technology innovations. There are many different types of instruments for measurement of radiation that are available. The basic requirement for each of these instruments is that its detector interact with radiation in such a manner that the magnitude of the instrument's response is proportional to the radiation effect or radiation property that is being measured. We will only discuss the solid state γ-ray and particle detectors.

13
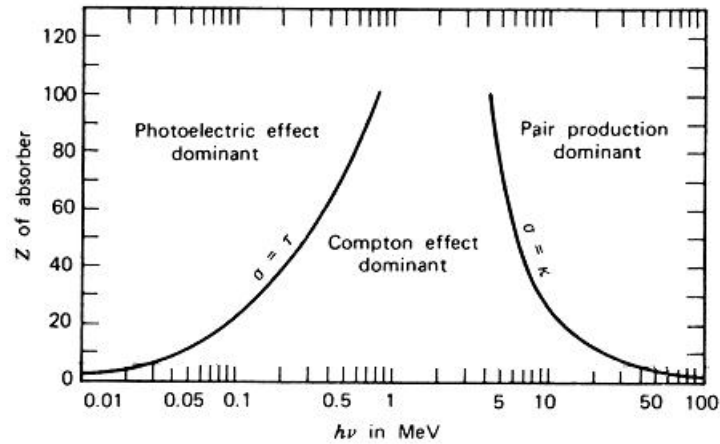
Figure 2.7: Illustration of the different regions where each of the three gamma-ray interaction processes dominates [14].

2.4.1 Scintillation Detectors

A scintillation detector is a transducer that changes the kinetic energy of the ionizing particle into a flash of light [17]. The various radiations may be detected with scintillation counters by using the appropriate scintillating material. Some examples of scintillating material include NaI(Tl), CsI(Tl), KI(Tl), etc. Solid state crystals are good for γ-ray spectroscopy because of their high detection efficiencies. Sodium iodide [i.e. NaI(Tl)] crystal activated with the impurity, thallium (at about 0.2%) is the frequently used compound for gamma-ray measurement. The high density of the crystal, together with its high effective atomic number, results in a high detection efficiency. The crystal is optically coupled to a photomultiplier tube.

The gamma-ray photons, passing through the crystal, interact with the atoms of the crystal by the usual mechanisms of photoelectric effect, Compton scattering, and pair production. The primary ionizing particles resulting from the gamma-ray interactions-the photoelectrons, Compton electrons, and positron-electron pairs, dissipate their kinetic energy by exciting and ionizing the atoms in the crystal. The excited atoms return to the ground state by releasing quanta of light. These light pulses cause electrons to be ejected from the cathode once they strike the photo-cathode of the photomultiplier tube. These electrons are then multiplied and focused by a series of electrodes, called *dynodes* along the photomultiplier tube. The dynodes are connected to a voltage, whose potential is about 100 V positive with respect to the photo-cathode. Each electron that strikes the dynode

14

causes more electrons to be ejected from the dynode, thereby leading to more gain in the number of electrons produced in each subsequent dynode. This leads to the multiplication of the original photo-current until all the electrons produced are collected by the plate of the photomultiplier tube. A current pulse, whose magnitude is proportional to the energy of the primary ionizing particle, can then be amplified and counted [14].

The major limitation of scintillation counters is that they have a relatively poor energy resolution, with $\Delta E_\gamma / E_\gamma \sim 5\%$ at best. This is due to the chain of events that must take place in converting the incident radiation energy to light and the subsequent generation of an electrical signal through a series of many inefficient steps. As a result, the best energy resolution from the most used radiation spectrometers is achieved using semiconductor detectors.

2.4.2 Semiconductor Detectors

A semiconductor is a substance that has electrical conducting properties that are halfway between a "good conductor" and an "insulator". Examples of solid semiconducting materials that are commonly used are germanium and silicon. Structurally these elements are characterized by having four valence electrons (group IV elements), which in their crystal lattice structure, all these valence electrons join together with the neighbouring atoms to form covalent bonds. In terms of the band structure of these elements, they have a filled valence band and an empty conduction band. These bands are separated
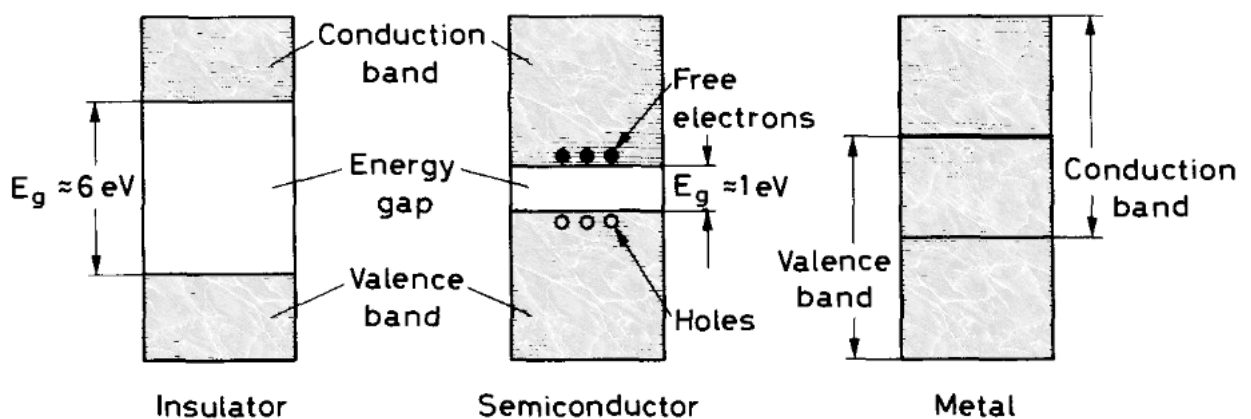
Figure 2.8: Energy band structure of insulators, semiconductors and metals (conductors) [18].

by regions, called *energy gaps*, where electrons are forbidden. The uppermost occupied energy band is the valence band, Figure 2.8. The conductivity of a material is determined by the occupancy of the valence band and the energy gap between it and the conduction band. Materials that are classified as insulators have a full valence band with the conduction band empty, but have a large energy gap (~6 eV) separating them. Semiconductors are similar to insulators, however they have a much smaller energy gap (~1 eV). If the valence band is only partially filled then the conduction band is effectively continuous with the valence band allowing a current to flow. Such types of materials are referred to as conductors (e.g. Metals) [18].

The absorption of energy by the crystal in semi-conductors leads to the excitation of electrons from the valence band across the energy gap to the conduction band. This results in a vacancy called a "hole" in the valence band. The free electron can move in the crystal with ease. The electron in the neighbouring atom fills the hole (thus creating another hole), the hole would appear to be as if migrating through the crystal. Connecting the semiconductor in a closed electric circuit results in a current through the semiconductor as the electrons flow towards the positive terminal and the holes flow toward the negative terminal. In *pure* semiconductors there is an equal number of electrons and holes produced and the material is referred to as an *intrinsic semiconductor*.

The operation of a semiconductor radiation detector depends on its having either an excess of electrons or an excess of holes. To achieve that, small amounts of materials called *dopants* are added to the semiconductor material such as germanium or silicon. These dopants which are normally group III or group V elements of the periodic table are introduced into the lattice structure of the semiconductor. Such types of materials whose semiconducting properties have been enhanced by the addition of an impurity are known as *extrinsic semiconductors*. If valence-3 atoms (e.g. boron, aluminium, gadolinium, or indium) have been introduced, three of the four valence bonds in the crystal lattice gets tied up. This deficiency of one electron is a hole, and a *p*-type silicon or germanium is formed. Alternatively, adding valence-5 atoms such as arsenic, bismuth, phosphorus, or antimony, each of which has five valence electrons, four of the five electrons in each of the added atoms are shared by the silicon or germanium atoms to form covalent bond. The fifth electron from the impurity (dopant) is an excess electron and is free to move about in the crystal and hence participate in the flow of electric current. This type of a silicon or germanium semiconductor is called an *n*-type.

If a *n*-type and *p*-type regions are put together, a *n-p* junction is formed. Applying a
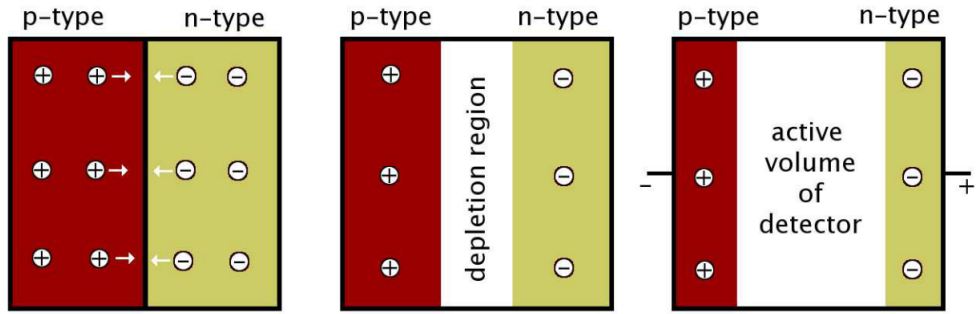
Figure 2.9: A diagrammatic representation of a p-n junction. Modified from [17].

forward bias to the junction i.e. applying a voltage across the junction with the n region connected to the negative terminal and the p region connected to the positive terminal, the electrons will diffuse across the junction into the p material combining with the holes. This results in a net positive charge in the n-type material and a net negative in the p-type material. Excess holes combine with excess electrons effectively cancelling each other out thus forming the *depletion region*. The depletion region illustrated in Figure 2.9, is the active element of the detector. If a reverse bias is applied across the junction, i.e. the n region is connected to the positive terminal and the p region is connected to the negative terminal, no current flows across the junction. Instead this increases the active volume of the detector, thereby increase the probability that radiation will interact with the detector. It also increases the magnitude of the electric field in the depletion region, making the charge collection more efficient.

2.4.3   High-Purity Germanium (HPGe) Detectors

High-Purity Germanium (HPGe) detectors have been used in gamma-ray spectroscopy for many decades now. Due to the high penetrating ability of the gamma-rays, a relatively large volume depletion region is necessary. The thickness of the depletion region is given by the expression [19]

$$d = \sqrt{\frac{2\epsilon V}{eN}},$$ (2.19)

where V is the reverse bias and N is the net impurity concentration. From this expression it is clear that decreasing the net impurity, N in your material will lead to an increase in the size of the depletion region, d. High-Purity Germanium detectors are made from germanium material whose purity levels are less than 10^9 atoms per cm^3. If the remaining

17

impurities in the semiconductor material are donor-type (having an excess of electrons), the crystal is referred to as n-type and if they are acceptor (with a deficiency of an electron i.e. having a hole), the crystal is called p-type.

In gamma-ray spectroscopy, the most common used detector configuration is the n-type coaxial configuration. In this type of coaxial configuration you have a cylindrical n-type Ge crystal with a negative bias contact (p^+) on the outer surface of the crystal and a positive bias contact (n^+) along the inside central axis of the crystal. One of the main advantages of the n-type HPGe detectors over the other type (the p-type) is that they show much less performance degradation from radiation damage [19]. Ge detectors are cooled to liquid nitrogen temperatures in order to reduce electrical noise from the leakage current due to thermal effects. With reverse biases of several thousand volts, leakage currents of less than 1na have to be achieved.

Clover Detectors

More recently composite detectors have been developed in order to provide better gamma efficiency and polarization sensitivity in gamma-ray spectroscopy [20]. A clover detector consists of four individual n-type germanium crystals closely packed together in the configuration of a four-leaf clover. These four germanium segments are housed in a single cryostat. Each crystal is tapered at one end to allow better positioning of the detector to the reaction centre thereby improve the overall efficiency of the detector. The clover detector is then coupled to an automatic LN_2 filling system which top up the dewars with LN_2 from the storage tank.

Some gamma-rays are Compton scattered from one segment to another segment of the clover detector. The energy detected in both segments can be added to obtain the full energy of the γ-ray. This enhances the photo-peak efficiency of the clover detectors especially for the γ-rays with high energy. The process is referred to as "addback".

LEP Detectors

Low-Energy Photon Spectrometer detectors consists of a single crystal of p-type HPGe. In AFRODITE each crystal is electrically segmented into four quadrants [21]. These detectors are also fitted with liquid nitrogen dewars (filled with liquid nitrogen) to keep them cold.
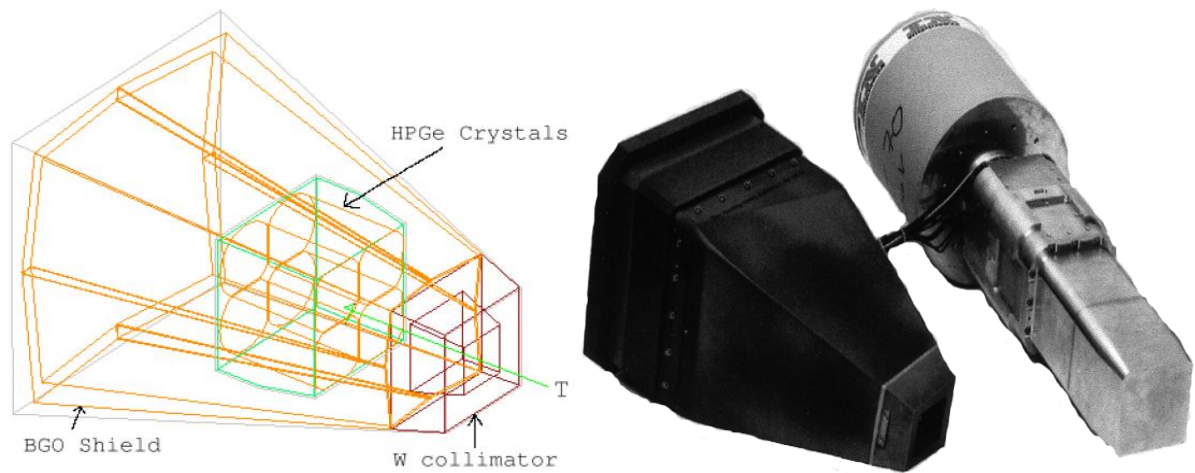
Figure 2.10: Clover detector showing a 3 dimensional-CAD view (left side) [22] and an exploded view (right side) [23]. Gamma-rays are produced at the target position (T) to the front face of the clover detector.

2.4.4 The Compton Suppression Spectrometer (CSS)

During gamma-ray detection not all gamma-rays deliver all their energy during the interaction in the detector volume. Some gamma-rays can Compton scatter out of the detector volume, thus leading to the gamma-ray's partial deposition of its energy in the detector. Such events are regarded to be bad events in the detector element. This produces a continuous background called *Compton background* in the spectra. This background is unwanted as it compromises the quality of the data. It introduces uncertainties into the intensities of the peaks and may even completely mask the weaker ones.

In order to improve the quality of spectra from a germanium detector one can use an escape suppression shield (see Figure 2.10). This shield, usually bismuth germanate (BGO) consists of a number of dense scintillation crystals which are wrapped around the germanium detector. The photons that Compton scattered off the germanium crystal can now be detected, and are rejected in the electronics. The rejection is done by passing the pulses from the germanium detector through an electronic logic gate that is closed if a coincidence pulse is detected from the surrounding detector. An unshielded germanium detector will normally have a peak-to-total (P/T) ratio of $\sim$20%, where only 20% of the counts are in the photo-peak and rest 80% are in the background. If the germanium detector is shielded, the P/T ratio is greatly improved to the region of $\sim$60% as illustrated in Figure 2.11.
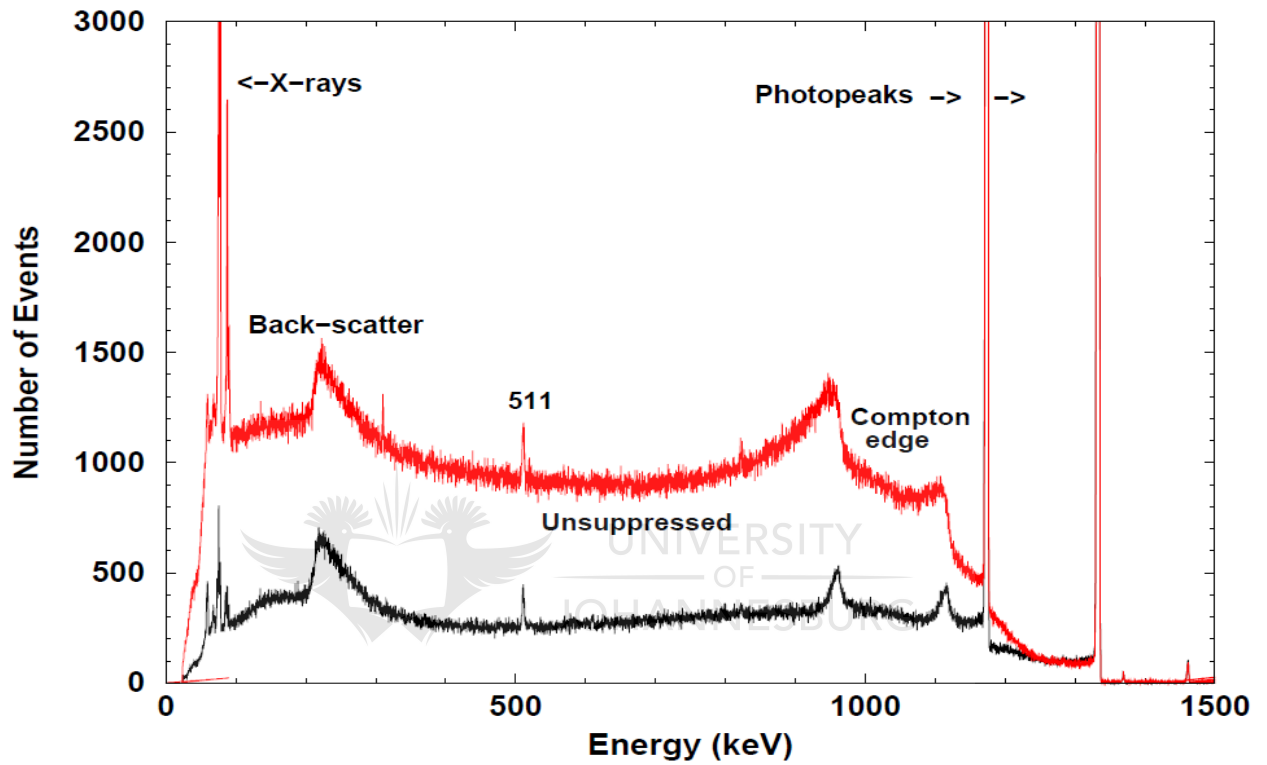
Figure 2.11: Spectra from a ^{60}Co γ-rays source showing the comparison between the unsuppressed spectrum and the suppressed spectrum measured with a clover detector [24, 23].

2.5   Array Construction

In order to increase the possibility of detecting as many gamma-rays as possible in a
nuclear reaction you need as many as possible HPGe detectors in a spherical (4π) config-
uration around the target chamber. This kind of detector set-up dramatically improves
the efficiency of the array. There are many arrays around the world with this physi-
cal set-up of detectors. These include arrays such as the GAMMASPHERE (consisting
of up to 110 HPGe detectors) originally at the Lawrence Berkeley National Laboratory
(USA) and now at Argone National Laboratory (USA), EUROBALL (consists of about
71 different germanium detectors), a joint European project, EXOGAM at the Grand
Accelerator National d'Ions Lourds in GANIL, Caen, France from which the AFRODITE
design was based on, and many others. The experiment in this paper was conducted using
AFRODITE coupled with DIAMANT (from Hungary) at iThemba LABS, Cape Town in
South Africa. However, it must be pointed out that the author did not participate in the
experiment but only received data to analyse.

2.5.1   AFRODITE

The AFRican Omnipurpose Detector for Innovative Techniques and Experiments (AFRODITE)
is an array consisting of two types of High Purity Germanium detectors, which are the
clover (for high energy gamma-rays) and Low Energy Photon Spectrometers (LEPS) de-
tectors [21]. These detectors are mounted in an aluminium frame which is rhombicuboc-
tahedron shaped, Figure 2.12.

Originally this frame was designed to accommodate up to a maximum of 16 detectors
with different combinations of the two sets of detectors, i.e. the clovers and LEPS, to
suit the measurement required. Two square facets positioned at 0°and 180°with respect
to the beam direction accommodate the beam line. The top most square facet supports
the hydraulic target positioner. The target-ladder is mounted on the hydraulic positioner
which can be controlled from the vault or control room. The rest of the square facets can
be used to mount detectors at different angles with respect to the beam line. Some of the
detailed specifications of the AFRODITE are given in Table 2.1.

For this experiment eight clover detectors were used, four of them were placed at 45°and
the other four at 90°with respect to the beam. The AFRODITE can also be coupled with
other ancillary detectors such as solar cells, neutron detectors, the recoil detectors, and
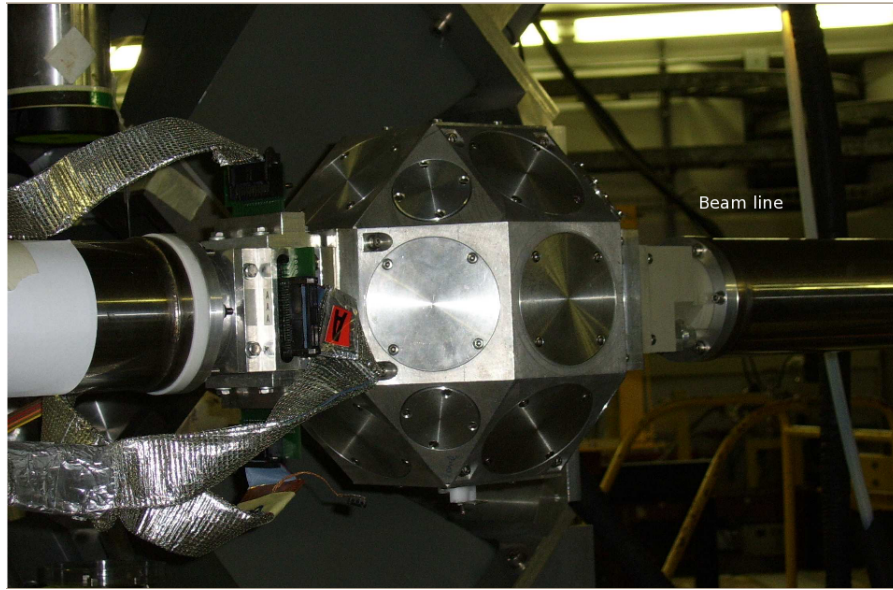
Figure 2.12: The rhombicuboctahedron-shaped target chamber has a total of 18 aluminium square facets and 8 triangular facets.
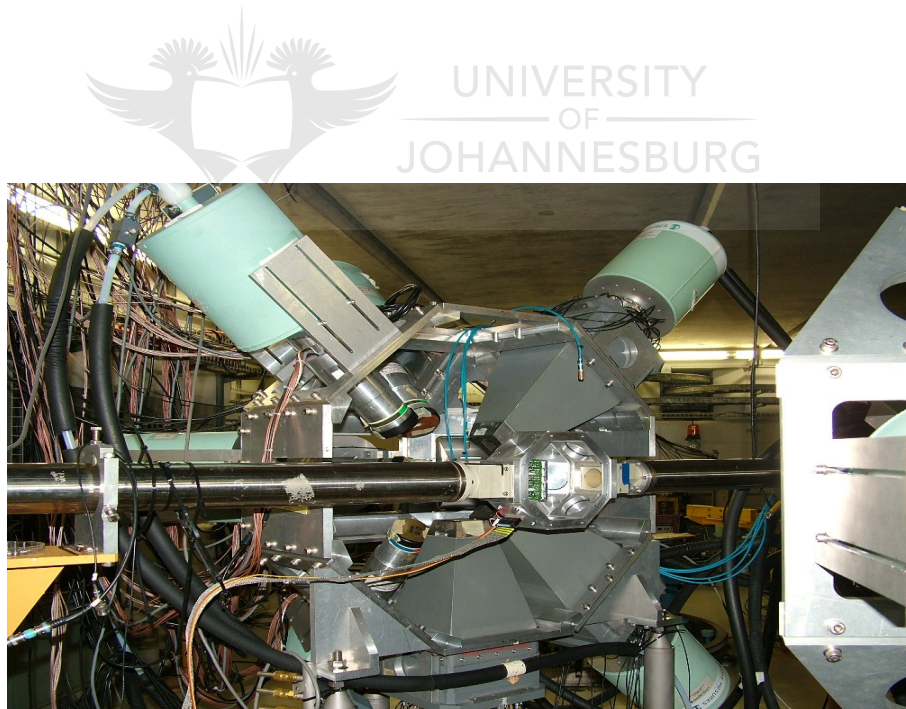
Figure 2.13: AFRODITE array with its frame supporting the clover and LEPS detectors.

DIAMANT as it is the case with this experiment.

Table 2.1: Some specifications of the AFRODITE [22].

Specification	Clover	Compton suppressors	LEPS
Supplier:	Eurisys	Crismatec	Eurisys
crystal type:	HPGe	BGO	HPGe
length:	71 mm[1]	$\sim$26 cm	10 mm
diameter:	51 mm[1]		66 mm[2],60 mm[3]
thickness:		$\sim$(4-20) mm	
taper angle:	7.1°	$\sim$8.1°	
L_{ec}^{7}:	20 mm		15 mm
entrance window:			119 mm[4]
total opening angle[4]:	23.2°		23.3°
detector solid angle[5]:	1.34%[6]		1.57%

[1]specification before shaping

[2]external

[3]associated with the active area

[4]for a 4 mm gap between target chamber and end-cap

[5]percentage of 4π

[6]for a 0.2 mm distance between crystals

[7]L_{ec} the distance from the detector end-cap to crystal surface

2.5.2   DIAMANT

DIAMANT is a 4π array of light charged-particle detectors [25, 26] involving 54 CsI(Tl) scintillators, 3 mm thick, which could be assembled in a quasi-spherical geometry, Figure 2.14. Each scintillator is coupled to a photodiode via an optical guide of plexiglass. It was developed to be used as an ancillary detector used inside large gamma-ray spectrometers to identify the light charged particles emitted in heavy-ion induced reactions. This was the arrangement that was used to collect time correlated particle-γ-γ coincidences when the ^{176}Yb target foil was bombarded with ^{7}Li ions, which were supplied at an energy of 50 MeV by the iThemba LABS cyclotron accelerator. In order to reduce the amount of scattered beam incident on the particle detectors, the detectors were shielded with $\sim$46 mg/cm^2 Aluminium absorber foils. A 4π light charged particle multidetector like
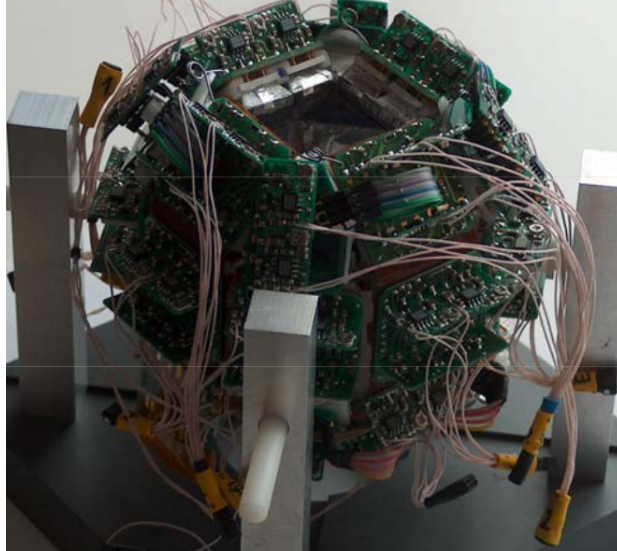
Figure 2.14: The DIAMANT flexi board on support stands ready for installation.

DIAMANT allows not only a channel selection, and then a higher sensitivity of the γ-spectrometer, but also can give additional information on the exit channel and the path leading to the final nucleus studied by its gamma emission.

DIAMANT consists of CsI(Tl) scintillation crystal detectors, which are equipped with charge sensitive preamplifiers working in a vacuum. The detectors are arranged in a polyhedron geometry. The processing of signals coming from the particle detectors is done by the VXI electronics. The VXI card contains eight complete electronic channels, each of which produces three signals: *energy, particle type* and *time reference*. The time reference gives the time relation between the signals arriving from the gamma and particle detectors. The particle type information is derived from the rise time of the input pulse and the energy information is given by the amplitude.

2.6 Offline Data Analysis

The very complex structure of the nucleus can, with great success, be explained using models that simplify the original problem. To test the validity of such models, experimental nuclear structure data are needed.

During the experiment, one has a limited freedom to interact with the data collection by inspecting and monitoring the process. These data are usually stored on magnetic tapes,

which are going to be used, firstly, to transfer the data to disk and secondly, used for archiving the data. The MIDAS [27] software DAQ package is used to record data in event-by-event mode. Once the data have been transferred, they must be organized into RADWARE [28, 29] readable format. This means sorting the data into symmetrized two-dimensional histograms, i.e. *matrices* from double coincidence data, or three-dimensional histograms, i.e. *cubes* from triple-coincidence data, or even *hypercubes* from quadruple-coincidence data.
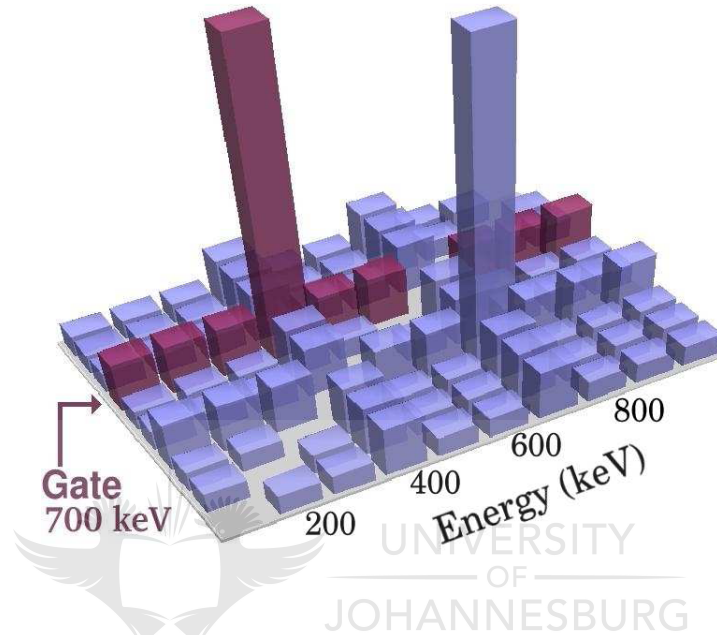
Figure 2.15: A typical γ-γ coincidence matrix with a gate set on 700 keV on the y-axis projected on the x-axis.

Each axis of the matrix/cube corresponds to the energy of the detected γ-rays. The number of counts in each (x,y) channel (in the matrix) is an indication of the number of pairs of γ-rays, that have been detected. Once the matrix, or cube has been built, the level scheme analysis can proceed. In this experiment the data was constructed into two-dimensional matrices, hence the ESCL8R code [28, 29] was used to analyse it.

2.6.1   Level Scheme Construction

In order to develop the theories of the nucleus and to be able to understand new phenomena, it is important to measure how excited states of the nucleus are distributed. One of the most important tools for studies of excited states in nuclei, is to study their decay via
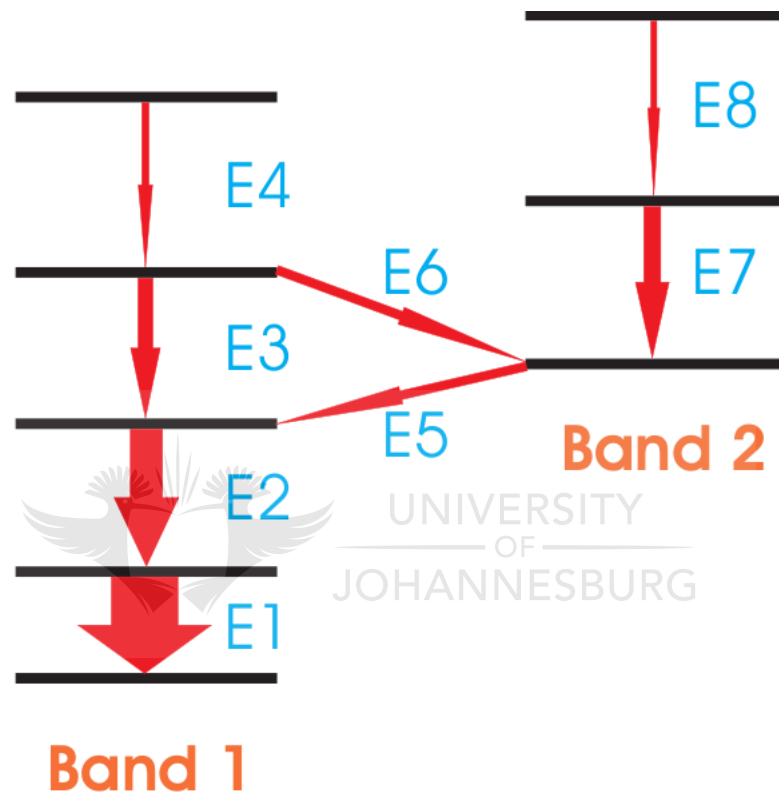
Figure 2.16: Part of a level scheme showing two rotational bands.

the emission of gamma-rays. The energy of the gamma-rays, also referred to as transition energy, gives the separation between the energy levels (excited states) of the nucleus.

If we can create the nucleus in an excited state, for example using a nuclear reaction or through alpha or beta decay, the nucleus is often de-excited by emission of a cascade of gamma radiation. This cascade connects different states with each other. If we use only one detector to detect the gamma decay we get a so-called *singles spectrum*, from which it is not possible to deduce anything about the relative positions of the energy levels. We only get a number of peaks in the spectrum which correspond to the energy differences between different states in the nucleus. In order to build up the *level scheme*, Figure 2.16 the de-excitation of the nucleus must in some way be related to each other. This is done by using at least two gamma-ray detectors in the experimental set-up, hence we have used AFRODITE (refer to Section 2.5.1), and demanding that these detect one gamma quantum each during a time gate with a length that is comparable to a typical lifetime of a nucleus.

By setting a gate (i.e. a narrow window) on one of the axes for an example on the y-axis at 700 keV in Figure 2.15 and projecting out the one dimensional γ-ray spectrum onto the x-axis, a coincidence spectrum is obtained. Moving horizontally along this spectrum, the row in red, these are peaks of various γ-rays that are in coincidence with 700 keV. By setting gates on the different peaks and examining the peaks in the gated spectra, it is possible to find out which gamma-rays belong to the same cascade (i.e. decay paths). From that, it is possible to determine the relative position of the energy levels, and how are they interconnected by the γ-ray transitions. If another nucleus happens to decay during the same time gate and as a result two or more γ-rays strike the same detector simultaneously, these results will fall outside the photo-peak. Such events are called *random coincidences* and give unwanted *background*. A high detector granularity is needed in order to avoid multiple hits on a single detector by more than one γ-ray from a cascade of emitted γ-rays. The number of detected events that are of this kind also depends on the number of gamma-rays that hit each detector per unit time. For an example, if the number of events in detectors 1 and 2 are R_1 and R_2 per second, respectively and the time gate is Δt seconds wide, on average there are $R_1 R_2 \Delta t$ random coincidences that are detected each second. By minimizing the time gate, this number can be kept at an acceptable level. In some cases a level is *metastable*, or *isomeric* as illustrated in Figure 2.17, which has consequence that all transitions that are below (or after) this level will end up outside this time gate if the gate is started by a transition above this level. In such a case, the

levels below and above the isomeric state are tied together by increasing the length of time gate.
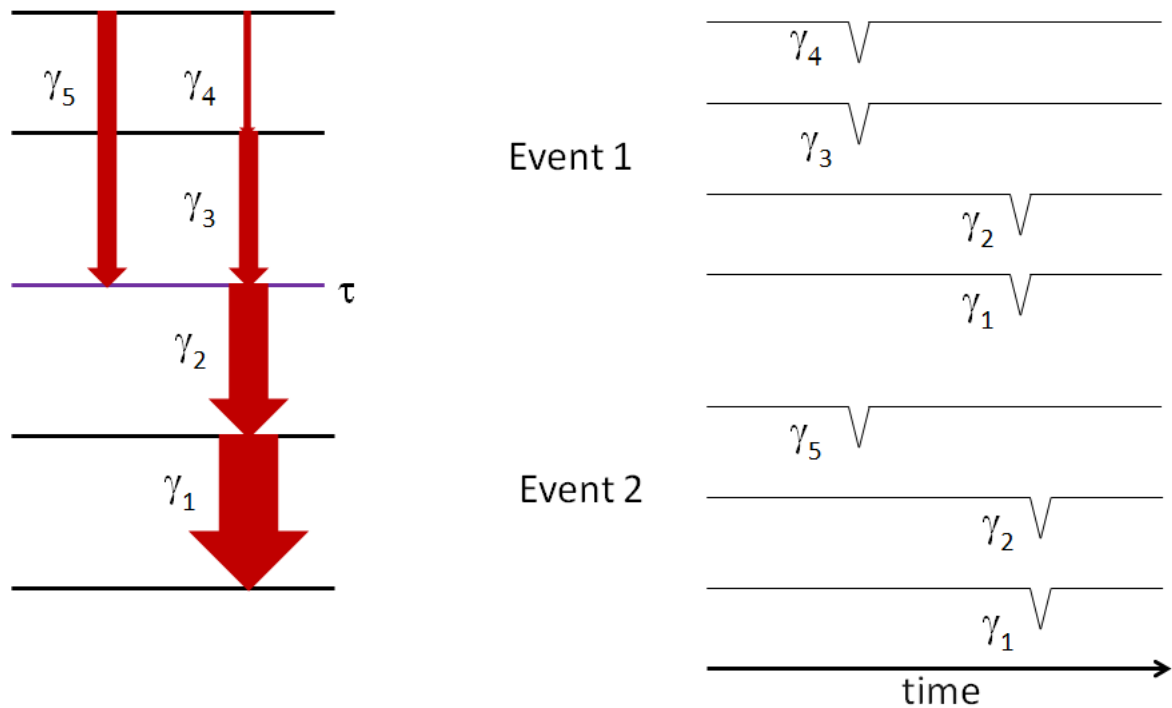
Figure 2.17: An illustration of decay scheme showing states that are isomeric in character.

The number of detected γ-rays in a single cascade is called *fold* and the total number of γ-rays emitted from a nuclear reaction is called γ-ray *multiplicity*. In these in-beam decay measurements the fold is typically around 1-8. If two γ-rays are detected in different detectors at approximately the same time they are said to be in *coincidence* with one another, are therefore interpreted as belonging to the same cascade from one de-exciting nucleus created in the reaction. In Figure 2.16, Band 1 gamma-rays E1, E2, E3 and E4 are all in coincidence with each other. This is the same as with E1, E2, E5, E7 and E8 gamma-rays constituting Band 2, they form same cascade. However, E5, E7 and E8 are anti-coincident with E3 and E4 gamma-rays. In these experiments the coincidence time condition between two γ-rays in a cascade is usually ± 100ns. This time condition is determined primarily by the time resolution of the detectors and their associated electronics and not by the nuclear state's lifetimes, which are usually much shorter, in the order of *ps*.

Assignments of Gamma Ray Multipolarities using DCO ratios

During fusion-evaporation reactions the nuclei absorb excitation energy and angular momentum, they become excited and some changes in their intrinsic structure can occur. Spins (I) and parities (π) associated with these excited levels in the level scheme, are essential in describing the structural behaviour of nuclei.

The Directional Correlation de-exciting Oriented states (DCO) method [30, 31], is often used when gamma-rays with small intensities are measured. In small arrays, such as the AFRODITE at iThemba LABS, the detectors are placed at only a few different angles, angles 45°, 90°and 135°with respect to the beam direction [32]. In this method, the intensities are measured in spectra where an anisotropic gate is set. An isotropic gate on a selected gamma-ray detected at 45°or 135°is set. Then the ratio of the intensities measured at 45°or 135°and 90°, given by

$$R_{DCO} = \frac{I_\gamma(45 + 135)}{I_\gamma(90)}, \tag{2.20}$$

is measured in the gated spectra for every γ-ray transition of interest and compared with the R_{DCO} for transitions with known multipole order. Gating on a stretched dipole transition gives ratios of $\approx$0.56 and for a pure stretched quadrupole transition gives ratios of $\approx$1.0. Mixed M1/E2 transitions can have a DCO ratio ranging from $\approx$0.3 up to $\approx$1.2. The gamma radiation from the decaying final nucleus is mostly of dipole or quadrupole nature or a mixture of both types.

The DCO ratios are unable to distinguish between the electric or magnetic nature of a γ-ray, therefore *linear polarization* measurements, explained in detail in [33], are performed. With DCO ratios combined with linear polarization, the multipolarity, parity and (electric or magnetic) nature of a γ-ray transition is determined.

Chapter 3

NUCLEAR STRUCTURE THEORY

3.1   Introduction

The main aim of nuclear theory is the eventual description of all nuclear properties in terms of the interactions of the constituent nucleons in a nucleus. However, the nucleus consists of a relatively large number of strongly interacting particles, and unlike the atom it is not obvious that there is any dominant central interaction such that the residual interaction between the particles can be treated as a small correction to the independent motion of the particles in the central field.

Due to the complexity of nuclear systems, a nuclear model attempts to deliberately simplify our study of the system and focus on particular features by constructing the model in such a way that it closely represents only those chosen features of the system. The reality contained in the detail is much too complicated for us to deal with the whole picture when we aim to investigate only one particular aspect. For any theoretical model to be useful it must not only explain previously observed phenomena, but should also provide insights into the system. The simplest nuclear model that one could think of is that of a nucleus as a solid charged sphere with a certain mass and diameter. That is suffice to describe correctly the elastic scattering of α-particles as was done by Rutherford. However, if we are going to describe the nuclear binding energy and some aspects of fission and fusion, the charged liquid drop model is a good approximation.

3.2 The Liquid Drop Model (LDM)

It was Rutherford's experiments in the early 1900s that revealed not only the evidence for a tiny, massive nucleus in the atom, but also properties of the nucleus itself. It was not until 3 decades later that the *charged liquid drop model* was developed, one which quantitatively described many nuclear properties quite well, especially the nuclear binding energy

$$E_B(A, Z) = \alpha A - \beta A^{\frac{2}{3}} - \gamma \frac{Z(Z-1)}{A^{\frac{1}{3}}} - \varepsilon \frac{(A - 2Z)^2}{A} + \delta(A, Z). \tag{3.1}$$

The model likens the nucleus to a macroscopic drop of charged liquid. The mass and the volume of the drop increase with the number of nucleons. The model was partly inspired by the observations that nuclear forces exhibit saturation properties. It was in 1935 when Weizsacker developed a formula for the binding energy as a function of atomic mass(A) and atomic number(Z) called the *Weizsaker semi-empirical mass formula*, given in Equation 3.1. The binding energy is due to the strong short-range nuclear forces that bind the nucleons together. It increases sharply as the mass number increases, peaking at iron (Fe) and then decreasing slowly for the more massive nuclei, Figure 3.1.

Each term in this formula has a definite theoretical basis. The first term, αA is proportional to the number of nucleons, which is proportional to the volume since nuclear matter is incompressible, hence this term is referred to as the **volume term**. The second term, $\beta A^{\frac{2}{3}}$ is the **surface term**. The nucleons at the surface of the "liquid drop" only interact with other nucleons inside the nucleus, so that their binding energy is reduced. This leads to a reduction of the binding energy proportional to the surface area of the drop, i.e. proportional to $A^{\frac{2}{3}}$. Another term which reduces the binding energy is $\gamma \frac{Z(Z-1)}{A^{\frac{1}{3}}}$, the **Coulomb term** which is the manifestation of the Coulomb repulsive forces between the protons in the nucleus. The electromagnetic force is long-range so each proton interacts with all the others and by Coulomb's law it is expected to be inversely proportional to the nuclear radius. The 4th term which also reduces the binding energy is $\varepsilon \frac{(A-2Z)^2}{A}$, the **asymmetry term**. This is a quantum effect arising from the Pauli's Exclusion Principle which only allows two protons or neutrons (with opposite spins) to occupy each energy state. If a nucleus has the same number of protons and neutrons then for each type the protons and neutrons fill to the same maximum energy level called *Fermi level*. If, on the other hand, one of the neutrons is exchanged with a proton then that proton would be required by the exclusion principle to occupy a higher energy state, since all the ones
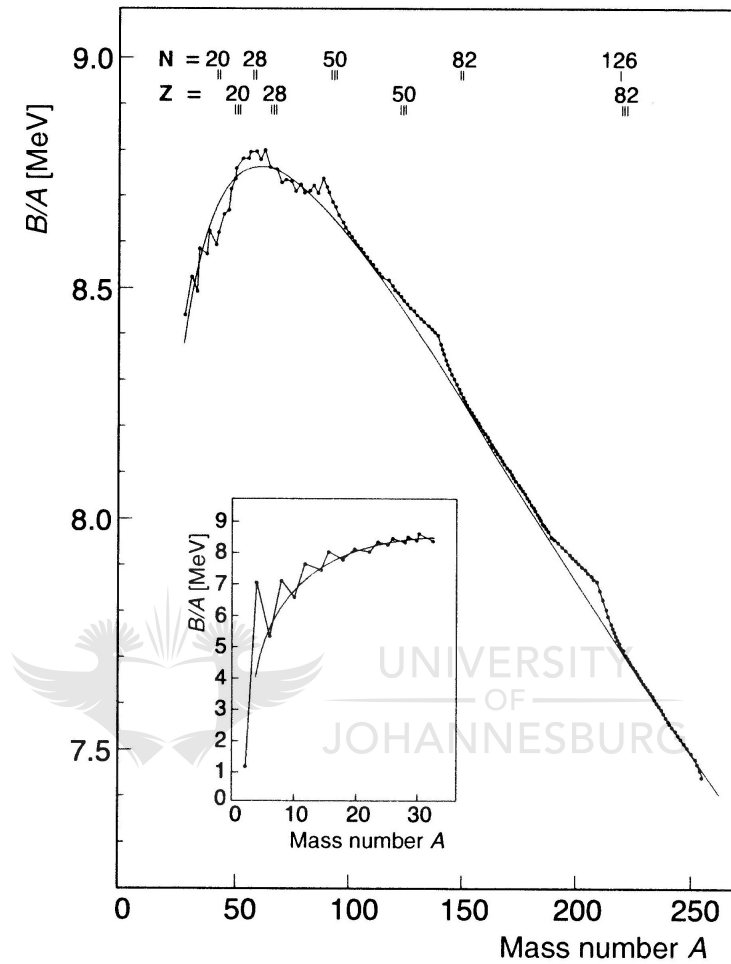
Figure 3.1: Average binding energy per nucleon as a function of nucleon number A for the most stable nucleus of each nucleon number. The solid line corresponds to the Weizsacker mass formula equation 3.1. The so-called "magic numbers" are indicated by points where the plot shows large deviation from the solid line [34].

32

below it are already occupied. It costs in energy to move up (that proton) the energy states. The last term in the semi-empirical mass formula, $\delta(A, Z)$ is the **pairing term**. Its been proven experimentally that two protons or neutrons bind more strongly than one proton and one neutron. To account for this experimental observation, the term is added to the binding energy if the number of protons and number of neutrons are both even, subtract the same term if these are both odd, nothing if one is odd and the other is even.

The liquid drop model predicts the average binding energy of the nucleons in the nucleus, however it fails to account for the observed systemic deviations in the average binding energy of some specific neutron and proton numbers such as 2, 8, 20, 28, 50, 82 and 126, the *magic numbers*. In order to explain some of these observed bulk property deviations the *shell model* was developed. In this model these can be explained by an increased binding energy for a full "closed" shell, analogous to the observed atomic electron shell closure.

3.3   The Spherical Shell Model (SSM)

The shell model [35, 36] considers the nucleus as a sequence of shells which can be occupied by nucleons. These nucleons move on almost undisturbed single-particle orbits within a nucleus. This requires a change of opinion from the previously established understanding of nuclei composed of constantly colliding nucleons. The Pauli's Exclusion Principle prohibits any possible collisions especially of the inner-shell nucleons, since all the nearby nuclear states are occupied [37]. Each particle of a given type (a proton/neutron) has a unique set of quantum numbers, forcing nucleons into higher energy states as shall be seen in the discussion later. In the model, the nucleons are governed by an average potential which is created by the presence of all nucleons within the nucleus

$$\left\{\frac{-\hbar^2}{2m}\nabla^2 + V(r)\right\}\psi(r) = E\psi(r) \tag{3.2}$$

$$V(r) = \frac{1}{2}kr^2 = \frac{1}{2}mw^2r^2. \tag{3.3}$$

The first step in developing the shell model is the choice of the potential, an attractive and manageable central potential. Next, solve the Schrödinger equation given in Equation 3.2 for the nucleon energy levels. In Equation 3.2, m is the particle mass, and r is the distance of the particle from the centre of the nucleus in the spherical coordinates. Consider two
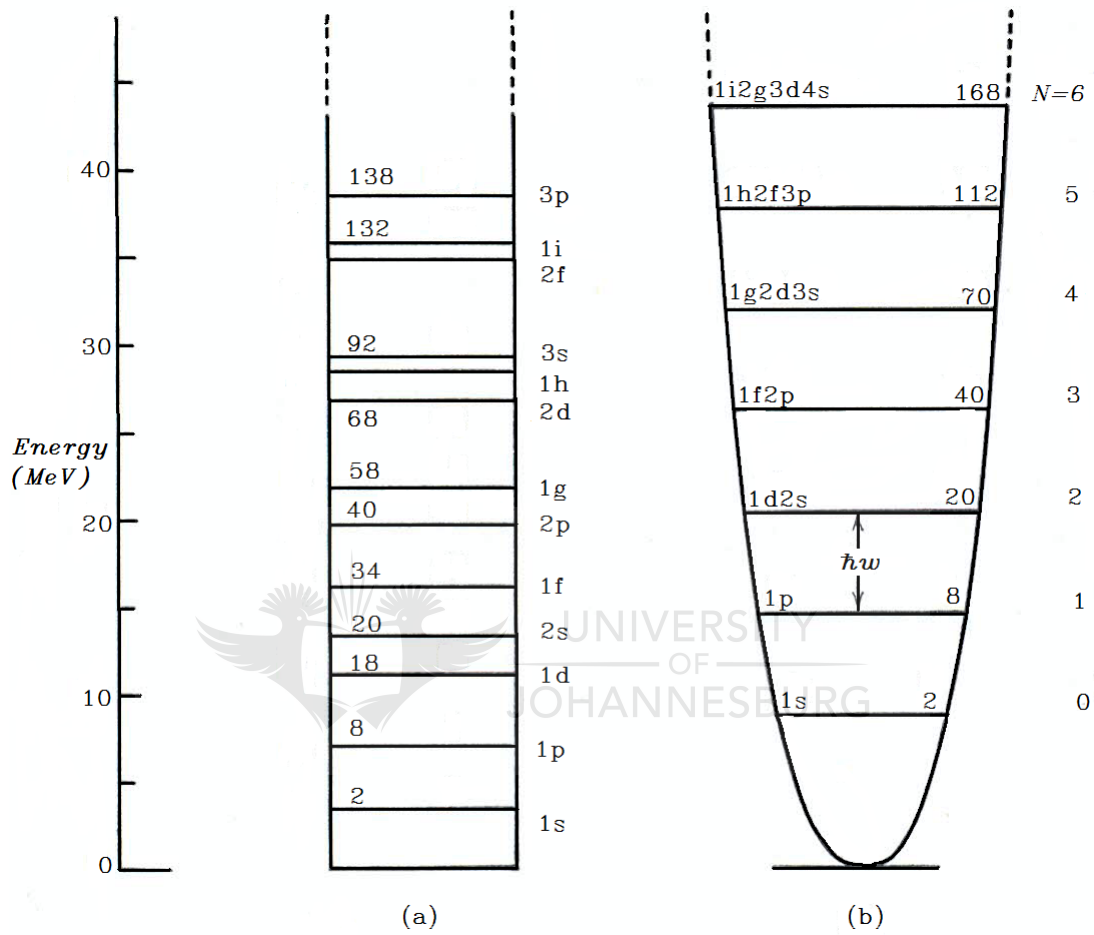
Figure 3.2: Level sequence for nucleons in a potential well, showing spectroscopic classification of levels and total number of nucleons on each level. (a) Infinite square well potential, (b) Harmonic oscillator potential with uniform spacing of levels [38].
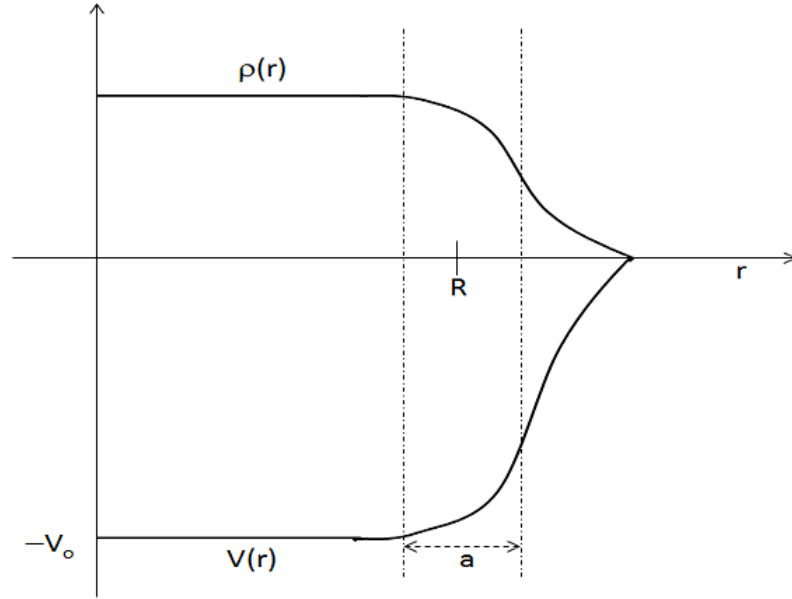
Figure 3.3: An illustration of the Woods-Saxon potential along density distribution [39].

potentials, an infinite square well whose potential is given by $V = 0$ inside the well and $V = \infty$ otherwise; and a simple 3-dimensional harmonic oscillator potential given in Equation 3.3. The solution of the Schrödinger equation yields the sequences of states given in Figure 3.2. The choice of the two wells turns out not to be a good approximation of the nuclear potential, since to separate a nucleon from these wells would need an infinite amount of energy. More over, the square well potential is an oversimplification as it has sharp edges which do not approximate the nuclear charge and matter distribution.

$$V(r) = -\frac{V_0}{1 + e^{(\frac{r-R}{a})}} \qquad (3.4)$$

An intermediate choice is the Woods-Saxon potential V_{WS}, which shows a similar shape to nuclear matter, Figure 3.3 [39]. It has an almost constant charge distribution within the nuclear radius and a smooth distribution to zero outside. The shape of the potential can be parametrized as given by Equation 3.4, where the parameters V_0, R and a are the depth of the potential, the mean nuclear radius and the surface thickness respectively. With the right fitted parameter values, this potential yields energy levels illustrated in Figure 3.4, the middle diagram. The energy values are occurring at 2, 8, 20, 40, 70, and 112 as the case with the harmonic oscillator potential in Figure 3.2(b). The first three of these values coincide with the known magic numbers but not the last three. Some modifications need to be done to the potential.
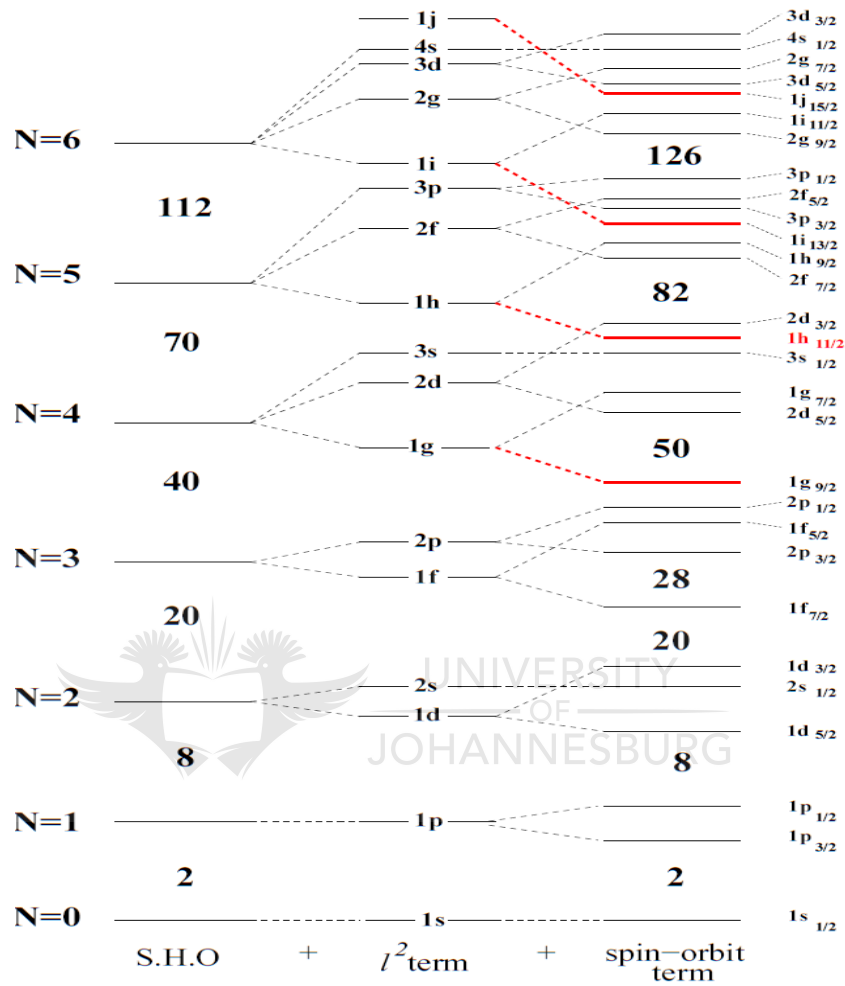
Figure 3.4: The evolution of single particle energies from a simple harmonic oscillator (S.H.O.) potential (left) to a realistic shell model potential, the Woods-Saxon potential with spin-orbit interaction included (right). The observed magic numbers are nicely reproduced for the latter case. The red lines illustrate intruder orbitals.

The potential is modified by the addition of a spin-orbit coupling force in analogy with atomic physics. It gives proper separation of the subshells, Figure 3.4, right. Nucleons, like electrons, have an intrinsic spin of $\frac{1}{2}\hbar$ (they are fermions). This makes the total angular momentum, j of a nucleon in any orbit to be given by the coupling of the orbital angular momentum l with a spin angular momentum, s. The energy of a state with given l, excluding $l = 0$ assumes two values, depending on the nucleon spin orientation relative to the direction of the orbital angular momentum, and the parallel orientation, $j = l + \frac{1}{2}$ corresponds to the lower energy and is $j = l - \frac{1}{2}$ otherwise. This means that instead of a single state nf, for an example, there will be two states $nf_{5/2}$ and $nf_{7/2}$. The degeneracy of each level i.e. the maximum number of protons or neutrons that the level/orbital can contain is given by $(2j + 1)$. Since protons and neutrons are two different particles they each have their own shell structure, giving rise to a classical picture seen in Figure 3.5. Here ^{16}O has 8 protons and 8 neutrons a *doubly magic* nucleus, has two particles, one of each spin, in the first level called S$_{1/2}$. This constitute the 1st shell. The second level, P$_{3/2}$ and third level P$_{1/2}$ both in the 2nd shell fit 4 and 2 nucleons respectively, and the scheme continues in a similar fashion.
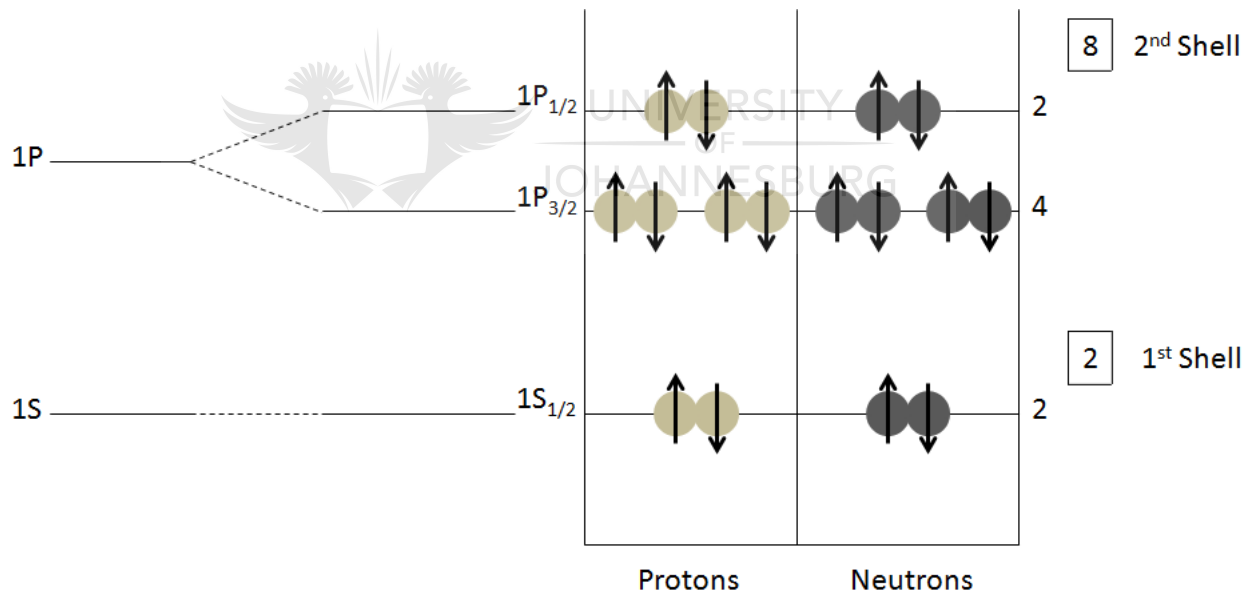
Figure 3.5: An illustration of shell model in ^{16}O. The states are labelled nlj (e.g. 1P$_{3/2}$), where $n = 1, 2, 3, ...$ is the number of a given l state, $l = s, p, d, f, g, h, i, ...$ describes the orbital angular momentum in the spectroscopic notation (the corresponding quantum numbers are $l = 0, 1, 2, 3, 4, 5, 6, ...$) and $j = l + s = l \pm \frac{1}{2}$ (s is the spin) is the total angular momentum quantum number of the orbital.

The energy splitting increases with increasing l. The inclusion of spin-orbit coupling reproduces the desired magic numbers. Also peculiar with the addition of spin-orbit coupling force to the potential is its effects on the level density in each shell. High-j orbitals are forced down in energy and as such reside amongst levels of the lower major oscillator shell as shown by lines highlighted in red in Figure 3.4. The lower shell has opposite parity therefore the *intruder* orbital does not interact with its opposite parity neighbours. These orbitals become significant as the nuclear potential becomes deformed and rotation is introduced, as will be shown in the next section.

The shell model is very successful in explaining nuclear excitation energies and their spin quantum numbers. It works well in low mass regions, where most nuclei are close to completed shells, however, at higher mass values, the huge amounts of computer power needed makes the approach infeasible without modification.

3.4 The Deformed Shell Model (DSM)

Experimental evidence shows that some nuclei are not spherical and are not near shell closures i.e. they are deformed. Mass numbers such as $A \simeq 25$, $150 < A < 190$ (nuclei of the rare earth metals) and $A > 220$, characterised by the large number of valence nucleons need a deformed potential to explain some of their nuclear properties. Such a deformed potential obtained from a modified harmonic oscillator potential was first introduced by Sven G. Nilsson [40, 41, 42]. It explains the observed features of single-particle levels in deformed nuclei. The total single-particle Hamiltonian for such a nucleus with axial symmetry (i.e. $\omega_x = \omega_y \neq \omega_z$) is given as follows [37]

$$
\begin{aligned}
H &= T + V \\
&= \frac{\mathbf{p}^2}{2m} + \frac{1}{2}m\left[\omega_x{}^2(x^2+y^2) + \omega_z{}^2 z^2\right] + \mathbf{C}l.s + \mathbf{D}l^2,
\end{aligned}
\tag{3.5}
$$

where m and $\mathbf{p}$ are the mass and momentum of the particle respectively, and the angular momentum (l^2) and spin-orbit $(l \cdot s)$ terms ensure the proper order and energies of the single-particle levels in the spherical limit. The shape of such non-spherical nuclei can be described in terms of spherical harmonics $Y_{\lambda\mu}(\theta,\phi)$ and shape parameters $\alpha_{\lambda\mu}$, which in essence are multipole expansion:

$$
R(\theta,\phi) = R_0\left[1 + \sum_{\lambda=1}^{\infty}\sum_{\mu=-\lambda}^{\lambda}\alpha_{\lambda\mu}Y_{\lambda\mu}(\theta,\phi)\right],
\tag{3.6}
$$

where R_0 is the radius of a sphere of the same volume as the non-spherical one, λ is the order of the expansion and α's are the expansion coefficients. The terms $\lambda = 1, 2, 3, 4$ correspond to dipole, quadrupole, octupole and hexadecapole deformation, Figure 3.6. The dipole term describes the displacement of the center-of-mass, which is given by $\alpha_{1\mu} = 0$ if the coordinates are constrained at the origin. The most common nuclear deformation is the quadrupole, which can be described by the following α's: α_{22}, α_{21}, α_{20}, α_{2-1}, α_{2-2}. With the quadrupole deformation, we can define the $\alpha_{\lambda\mu}$ to be in the coordinate system
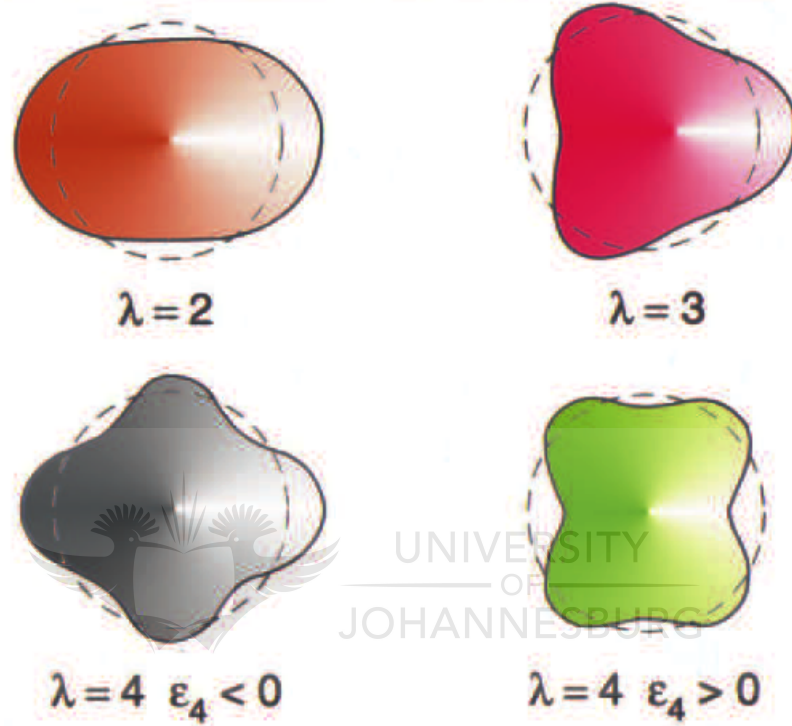
Figure 3.6: Various nuclear deformations, with $\lambda = 2$, 3 and 4 corresponding to quadrupole, octupole and hexadecapole deformation respectively. Modified from [37].

defined by the principal axes fixed in the frame of the nucleus, so that: $\alpha_{22} = \alpha_{2-2}$ and $\alpha_{11} = \alpha_{1-1} = 0$. According to the *Lund convention* [43] , see Figure 3.7, parametrization of the deformation uses (β_2, γ) defined by:

$$\alpha_{20} = \beta_2 cos\gamma \qquad (3.7)$$

$$\alpha_{22} = \frac{1}{\sqrt{2}}\beta_2 sin\gamma, \qquad (3.8)$$

where the parameter β_2 measures the total deformation while γ measures the lengths along the principal axes. The $\gamma = 0^0$ axis corresponds to a **prolate** shape and the $\gamma = 60^0$ axis corresponds to an **oblate** shape with the z-axis as the symmetry axis.
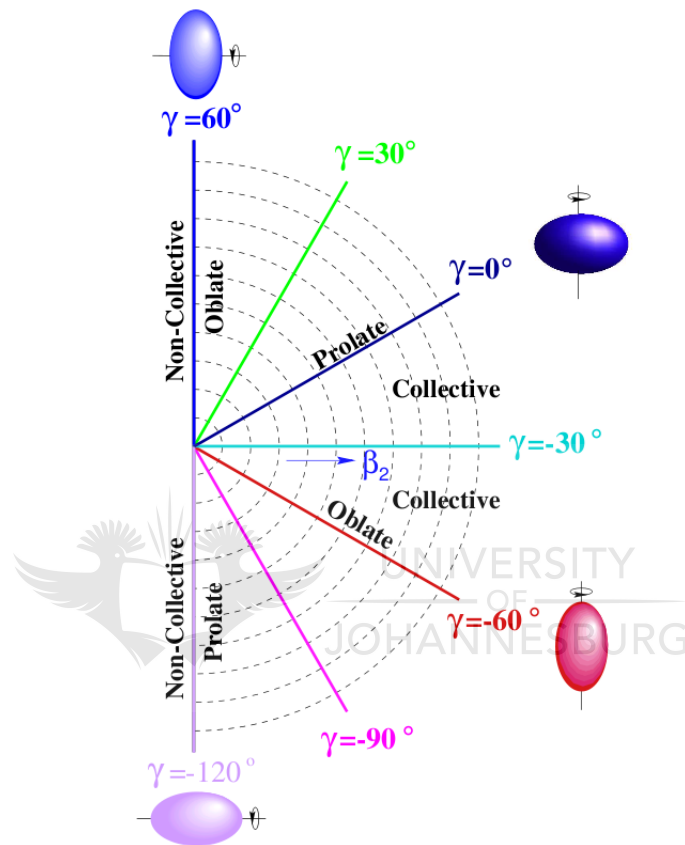
Figure 3.7: The Lund convention for describing quadrupole ($\lambda = 2$) shapes in the (β_2, γ) plane [43].

$$\Omega^{\pi}[Nn_z\Lambda] \hspace{4cm} (3.9)$$

Energy states in the Nilsson model are defined with the quantum numbers given in
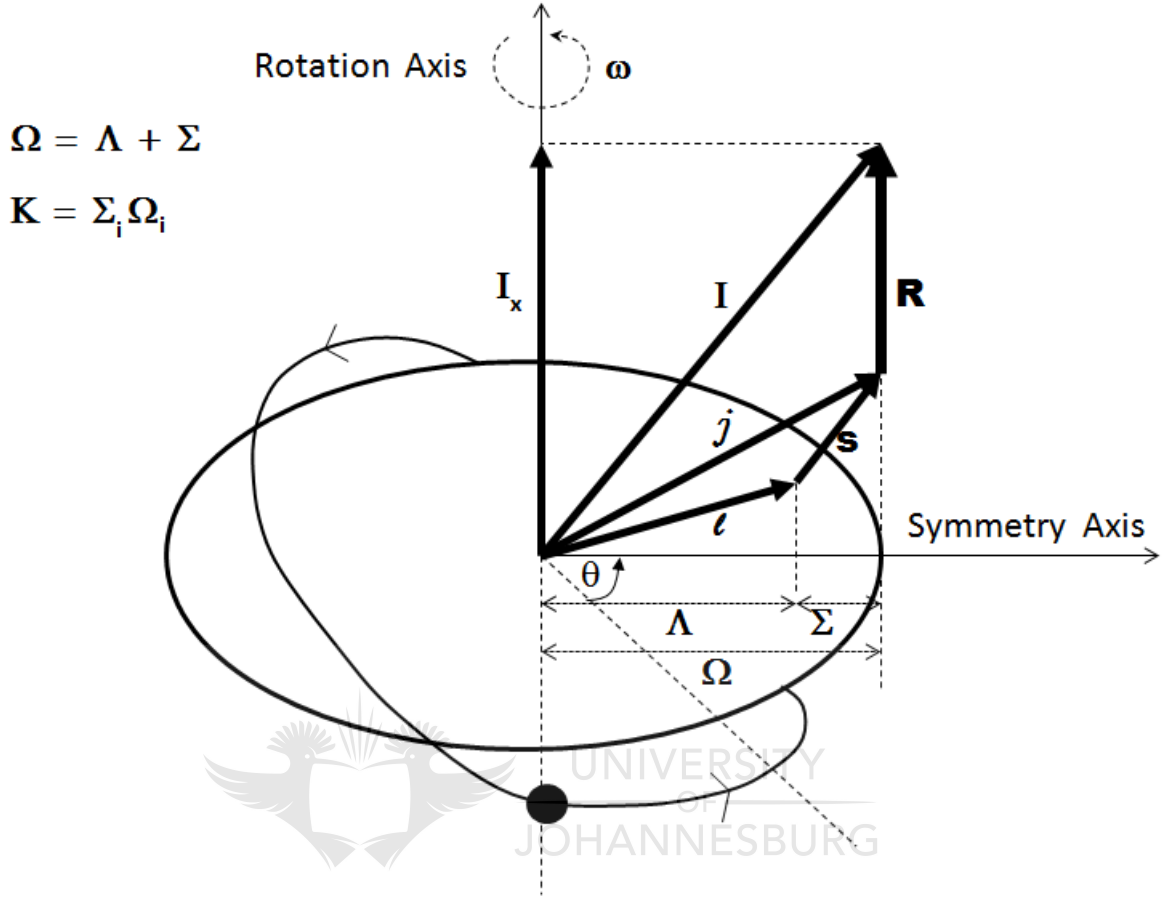
Figure 3.8: Illustration of a valence nucleon orbiting around a prolate-deformed nucleus. Z-axis is the axis of symmetry whereas X-axis $\perp$ to Z-axis is the axis of rotation. The nucleon has an orbital angular momentum $\vec{l}$ and spin $\vec{s}$. J is the total angular momentum such that $\vec{j} = \vec{l} + \vec{s}$. The projections of these vectors $\vec{j}$, $\vec{l}$ and $\vec{s}$ onto the Z-axis (the symmetry axis) are defined by Ω, Λ and Σ quantum numbers respectively. θ is the angle of the orbital plane.

the Expression 3.9. Ω is the projection of a single-particle angular momentum on the symmetry axis and π is the parity. The projection of the total angular momentum is defined as follows: $\Omega = \Lambda + \Sigma = \Lambda \pm \frac{1}{2}$, where Λ is the projection of the particle orbital angular momentum $\vec{l}$ onto the symmetry axis and Σ is the projection of the intrinsic nucleon spin $\vec{s}$ on the symmetry axis, Figure 3.8. N is the principal quantum number associated with the major shell to which the orbital belongs and determines the parity as

$(-1)^N$, n_z is the number of nodes in the wave-function along the direction of the symmetry axis. Orbital angular momentum l and the spin s quantum numbers are no longer good quantum numbers in the deformed shell model because they are not conserved. Only the Ω and π quantum numbers are conserved in the Nilsson model, hence are good quantum numbers. N, n_z and Λ are only good at asymptotically large deformations.
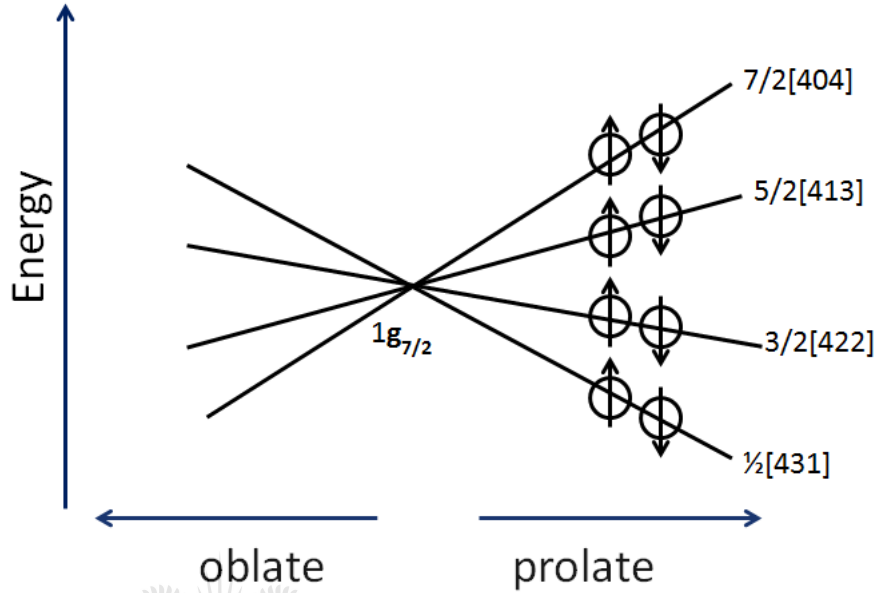
Figure 3.9: The 4 sub-states of the $j = \frac{7}{2}$ orbital are split based on the projection, Ω, on the symmetry axis [37].

The Nilsson model considers that a nucleus can be deformed in two possible ways: *prolate*, where the nucleus is stretched like a rugby ball, and *oblate* where the nucleus is compressed from opposite sides like a pancake. The nuclear energy levels are split into $(2j + 1)/2$ levels. The energy of each orbit depends on its orientation with respect to the axis of symmetry of the nucleus. In prolate quadrupole deformed nuclei, low K-values orbit along the equatorial plane, near the bulk of the nuclear matter, and as such have lower energy. In oblate nucleus the converse is true. Each level is now double degenerate, Figure 3.9. This lowering of degeneracy from $(2j + 1)$ in spherical case, to two for non-spherical case results from the breaking of spherical degree of symmetry.

Figure 3.10 shows Nilsson single-particle energies for protons in region $50 \leqslant Z \leqslant 82$. Each line, represents a Nilsson state, with the solid lines having positive parity and the dotted ones representing wave functions with negative parity. The orbitals with the same Ω^π
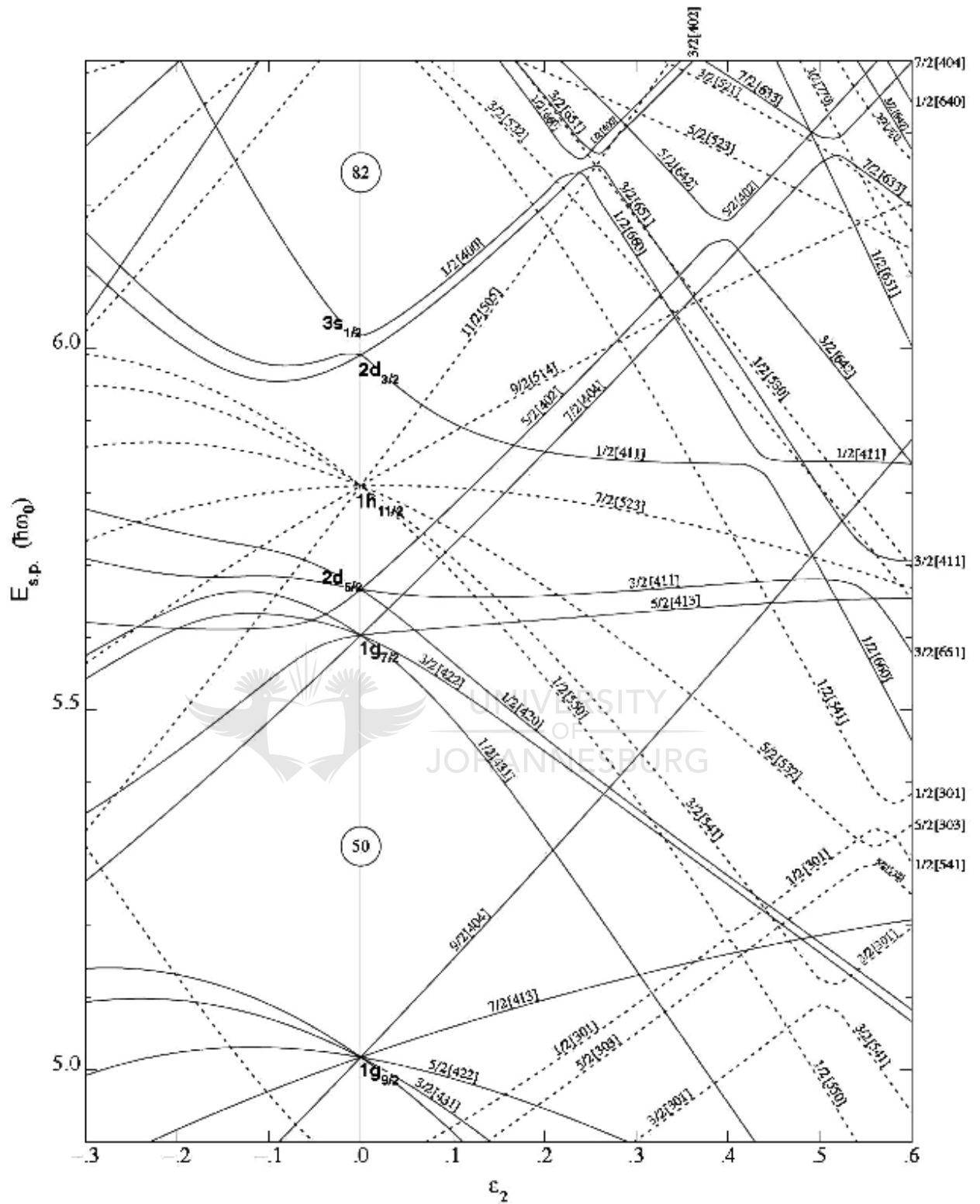
Figure 3.10: Nilsson orbitals for protons, $50 \leqslant Z \leqslant 82$. The level ordering is given as a function of the quadrupole deformation parameter, ε_2.

quantum numbers repel as they approach each other (e.g. 3/2[301] and 3/2[541] at $\varepsilon_2 \sim$ 0.5) due to the Pauli principle. The properties of the levels get interchanged at the crossing point and the wave functions corresponding to the two levels far from the crossing point are the same as if there had been no interchange at all. The point at where the lines would have crossed is called the *inflection point*.

Figure 3.11 shows a summary of all the shell models we have described in this work, with their associated degeneracies and quantum numbers.
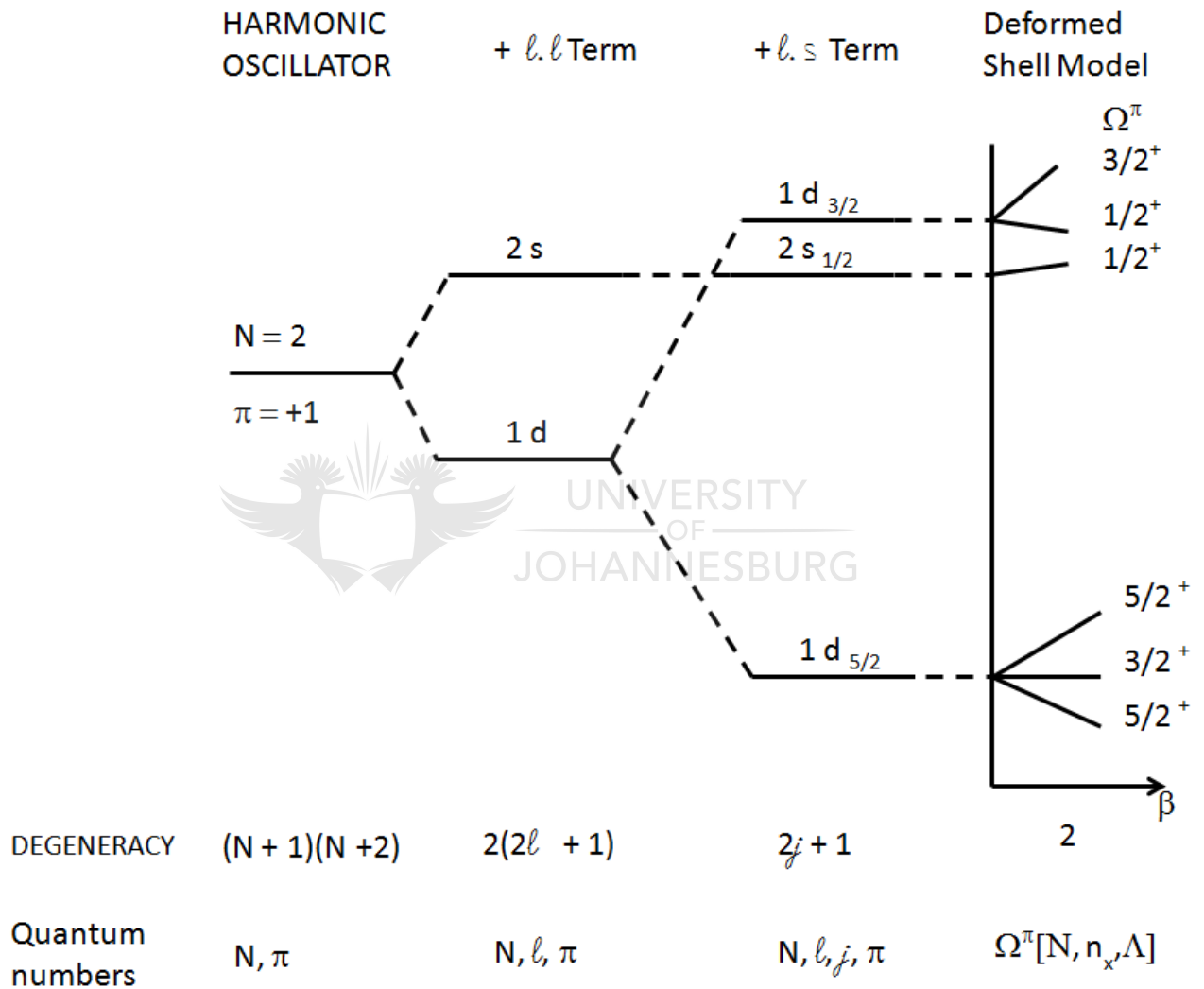
Figure 3.11: A summary of the development of the shell model.

3.5 Angular Momentum Generation

A nucleus can generate angular momentum mainly in two different ways i.e. by *collective* means via rotation and vibration or by few-nucleon excitations in which a small number of unpaired nucleons generate the angular momentum, the *non-collective* means. Generation by collectivity implies that many nucleons participate collectively in the generation of angular momentum.

3.5.1 Nuclear Rotations

One of the important consequences of deformation is the fact that rotational motion is a possible mode of excitation in the nucleus [44]. In spherical nuclei, it is not possible to observe collective rotation, since the orientation of the nucleus is undefined.

$$\mathbf{I} = \mathbf{R} + \mathbf{J} \tag{3.10}$$

For deformed axially symmetric nuclei, the total angular momentum, $\mathbf{I}$, is composed of two parts. The first is the angular momentum generated by the collective rotation, $\mathbf{R}$ and the second, that generated by the intrinsic motion of the individual valence nucleons, i.e.

$$\mathbf{J} = \sum_{i=1}^{valence} \mathbf{j}_i. \tag{3.11}$$

If you have only one valence nucleon ($i = 1$), Equation 3.11 reduces to $\mathbf{J} = \mathbf{j}$. The projection of the total angular momentum $\mathbf{I}$ onto the symmetry axis, is K, and is the same projection of $\mathbf{J}$. As was given earlier (in Section 3.4) on $K = \sum_{i=1}^{valence} \Omega_i$. The projection of $\mathbf{I}$ onto the rotation axis is denoted by I_x, and is known as the *aligned angular momentum*. It is given by the equation:

$$I_x = \left[\sqrt{I(I+1) - K^2} \right] \hbar. \tag{3.12}$$

The rotational energy of a rigid body for a classical rotation is given by:

$$E_{rot}(I) = \frac{1}{2} \mathscr{I} w^2, \tag{3.13}$$

where $\mathscr{I}$ is the moment of inertia and w is the angular frequency of the rotation. By using the angular momentum relation $\ell = \mathscr{I} w$, Equation 3.13 reduces to [14]

$$E_{rot}(I) = \frac{\ell^2}{2\mathscr{I}}. \tag{3.14}$$

45

In quantum mechanics the expectation value for the square of the angular momentum is given as $\langle \ell^2 \rangle = \ell(\ell+1)\hbar^2$. Substituting I for the angular momentum quantum number ℓ, gives

$$E_{rot}(I) = \frac{\hbar^2 I(I+1)}{2\mathscr{I}}. \tag{3.15}$$

Equation 3.15, gives energy values of states for a rotating object in quantum mechanics. Increasing the spin I is equivalent to adding rotational energy to the nucleus. For a perfect, idealised axially symmetric deformed even-even nucleus, the rotational levels take the following energy values [37, 14]:

$$E(0^+) = 0 \tag{3.16}$$

$$E(2^+) = 6\frac{\hbar^2}{2\mathscr{I}} \tag{3.17}$$

$$E(4^+) = 20\frac{\hbar^2}{2\mathscr{I}} \tag{3.18}$$

$$E(6^+) = 42\frac{\hbar^2}{2\mathscr{I}} \tag{3.19}$$

$$E(8^+) = 72\frac{\hbar^2}{2\mathscr{I}}, \tag{3.20}$$

and so on. Thus for an even-even axially symmetric deformed rotating nucleus whose $K = 0$, the energy ratio $E(4^+)/E(2^+)$ should approximately be equal to 3.33, for a spherical vibrational nucleus, the ratio is ~ 2.0 and a triaxial rotor, ~ 2.5 [37]. The nuclear excited states should cascade down toward the ground state, through a sequence of $E2$ γ transitions, known as a *rotational band*. The γ-ray transitional energies are given by the difference in energy between sequential states ($I \rightarrow I$-2):

$$
\begin{aligned}
E_\gamma &= \Delta E_{rot} \\
&= E_{rot}(I) - E_{rot}(I-2) \\
&= \frac{[I(I+1) - (I-2)(I-2+1)]\hbar^2}{2\mathscr{I}} \\
&= \frac{(4I-2)\hbar^2}{2\mathscr{I}}. \tag{3.21}
\end{aligned}
$$

For a band with a non-zero K value, Equation 3.15 becomes,

$$E_{rot}(I) = \frac{\hbar^2}{2\mathscr{I}}\left[I(I+1) - K^2\right]. \tag{3.22}$$

The single-particle angular momentum $\mathbf{j}$ for an odd-A nucleus can couple to the rotational angular momentum of the deformed nuclear core in two ways. At low rotational frequencies and the deformation in the nuclear field is large enough, the valence nucleonic

motion is coupled to the deformation of the core. The angular momentum of the valence nucleon is aligned with the symmetry z-axis. This extreme coupling limit is called the *strong* or *deformed aligned* (DAL) scheme, Figure 3.12. In this case the spin values of the rotational band are given by

$$I = K, K+1, K+2, K+3, ... \qquad (3.23)$$
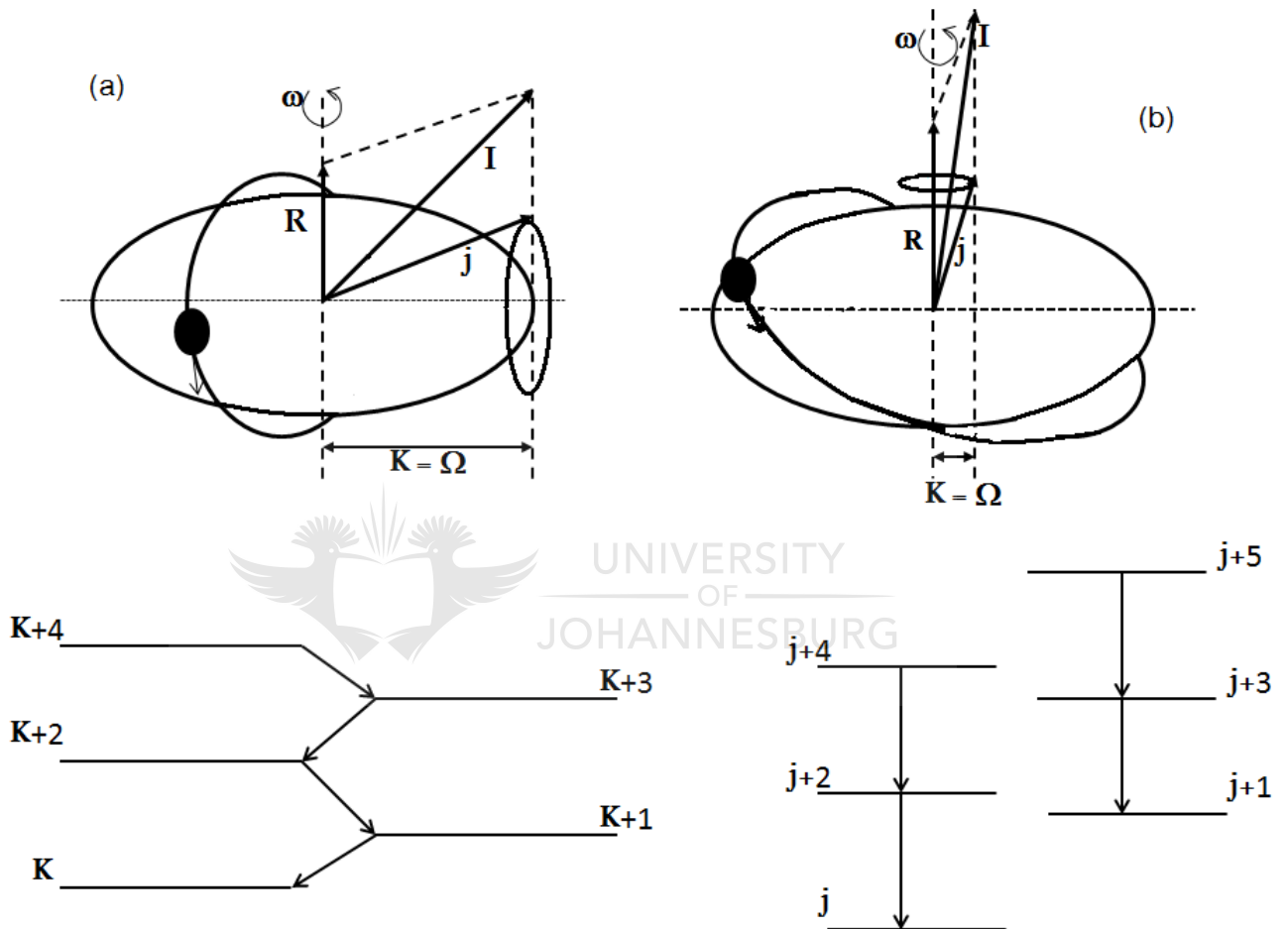
Figure 3.12: Angular momentum coupling schemes for a valence nucleon coupled to a rotating nuclear core, with (a) representing the *strong* or *deformed aligned* (DAL) and (b) the *weak* or *rotational-aligned* (RAL) scheme. Shown below are their typical rotational band structures in each case [16].

However, if the odd nucleon moves in a very weakly deformed field and the rotation is fast enough, at a critical frequency $\omega_{crit.}$, Coriolis forces may be strong enough to dominate the particle motion. The nucleonic angular momentum j may become completely aligned

47

with the angular momentum of the rotating nuclear core and as a result, the nucleonic orbit is roughly located in the plane perpendicular to the rotation axis. The nucleon's motion is now de-coupled to the rotation of the core and this scheme represents the *weak* or *rotational-aligned* (RAL) scheme. Coriolis forces in deformed nuclei, are particularly significant for orbitals with high-j and low-Ω. The Coriolis operator on a single orbiting particle is given by the expression [45]

$$-2\frac{\hbar^2}{\mathscr{J}}(\mathbf{I}.\mathbf{j} - \Omega^2). \tag{3.24}$$

The spin values of the *yrast* band members are determined by the properties of the even core, with the particle angular momentum j being added in a parallel way to that of the core. The resulting spin sequence becomes [9]

$$I = j, j + 2, j + 4, ... \tag{3.25}$$

Ground State Angular Momentum Coupling in Odd-Odd Nuclei

The last single proton and neutron in odd-odd nuclei can be classed as being paired. The ground state spins of some odd-odd nuclei can be accounted for on the basis of a $j - j$ coupling model with some certain simple rules controlling the coupling of angular momentum of the last odd proton and neutron [46, 47]. These rules are as follows:

$$
\begin{aligned}
I &= j_p + j_n & \text{if} \quad j_p &= l_p \pm \frac{1}{2} \quad \text{and} \quad j_n &= l_n \pm \frac{1}{2}; \\
I &= |j_p - j_n| & \text{if} \quad j_p &= l_p \pm \frac{1}{2} \quad \text{and} \quad j_n &= l_n \mp \frac{1}{2},
\end{aligned}
\tag{3.26}
$$

where j_p, and l_p (or j_n and l_n)represent the total and orbital angular momentum of the odd proton p and neutron n deduced from the neighbouring odd-A nuclei. However, in the case of nuclei which have protons (or neutrons) one above or below a closed shell these rules do not hold. In this case the ground-state angular momentum is given by the following:

$$I = j_p + j_n - 1. \tag{3.27}$$

48

3.5.2 Nuclear Vibrations

β vibrations   γ vibrations

Dipole   Quadropole vibrations   Octupole vibrations
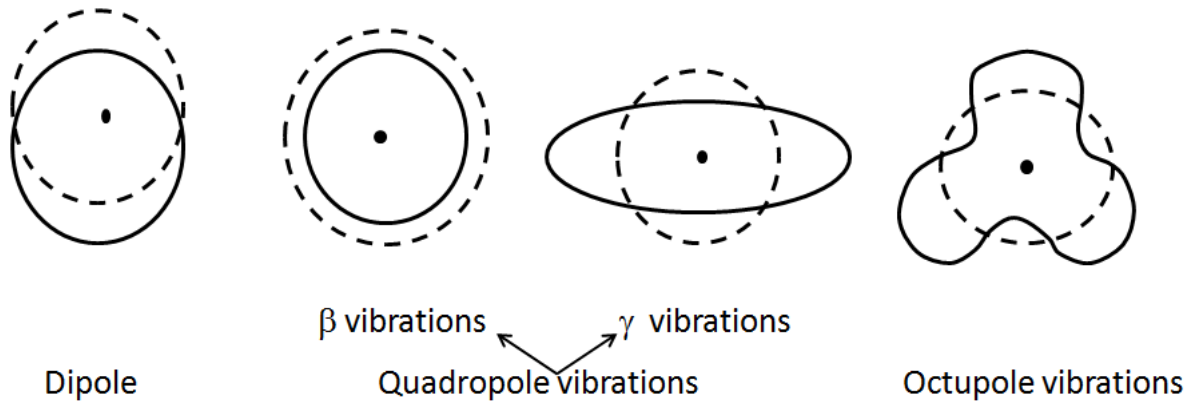
Figure 3.13: Diagram showing the lowest three vibrational modes of a nucleus. Modified from the source [14].

Vibrational modes of excitation are described in terms of phonons. They (the phonons) are described by defined multipolarity, λ. A $\lambda = 1$ deformation corresponds to a collective electric dipole excitation, which represents a shift of the centre of the mass of the nucleus.

The quadrupole ($\lambda = 2$) excitation is the next lowest order of vibrational mode. The phonons of $\lambda = 2$ can take two forms, Figure 3.13. The first, β vibrations which are shape oscillations directed along the symmetry axis. The angular momentum vector for such oscillations is perpendicular to the symmetry axis, therefore such bands are based on $I^\pi = K^\pi = 0^+$ states. The parity being determined by $(-1)^\lambda$. The second type, are γ vibrations whose oscillations are perpendicular to the symmetry axis. Their angular momentum vector, the γ vibrations, points along the symmetry axis , which gives rise to bands based on $I^\pi = K^\pi = 2^+$ states [37].

Octupole vibrations are associated with $\lambda = 3$ phonons. The shape that arises from this mode of excitation may be viewed as a standard pear-shape type of vibration. These oscillations yield bands based on $K^\pi = I^\pi = 0^-, 1^-, 2^-$ and 3^- states.

3.6 Electromagnetic Decay

Each nucleon in the nucleus has quantized orbital and spin angular momentum, and both contribute to the total angular momentum (i.e. spin) of the nucleus I. The vector coupling
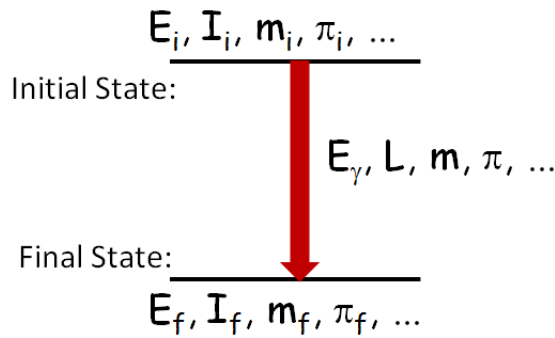
Figure 3.14: Electromagnetic transition from an initial level to a final level.

of these angular momenta produce many different states of the nucleus with different values of I and different energies. From Figure 3.14, each energy state with spin I is also associated with $2I + 1$ magnetic substates m. Nucleons have an intrinsic spin $s = \frac{1}{2}$, which implies that for an even number of nucleons in a nucleus, the possible values of I are integers, while for an odd number of nucleons, the possible values of I are half integers. An additional quantum number, parity π, is associated with each state. The parity is either positive or negative 1, and defines the response of the wavefunction to the sign inversion of its constituent position vectors. These quantum numbers are experimentally measured and thus it becomes possible to deduce nuclear structure changes when the nucleus is in an excited state.

When the nuclei acquire energy and angular momentum, they become excited and some changes occur in their intrinsic structure. The excited states usually live for a short period of time (typically in the *ps* range) and decay by emitting gamma-rays. There is no change in the nucleus as regards to the number of protons and the number of neutrons, but the emission of a γ-ray photon removes energy, enabling the nucleus to undergo a transition to a lower energy, thus (usually) a more stable state. The gamma-rays carry information about the nuclear transition from the initial level to the final level, Figure 3.14, such as what amount of energy, angular momentum, parity, etc. is taken away. These gamma-rays are detected and studied (i.e. gamma-ray spectroscopy) in order to determine the properties of the excited states.

A gamma-ray is an electromagnetic wave. Every electromagnetic wave consists of a oscillating electric field and magnetic field. The oscillating electric field of the gamma-ray is caused by an oscillating charge whereas the oscillating magnetic field is caused by an oscillating electric current. In the first case the radiation induced is called *electric multipole*

radiation (EL) and the second case it is called *magnetic multipole* radiation (ML).

3.6.1 Selection rules for Gamma Decay

Consider a γ-transition from an initial excited state of energy E_i, angular momentum I_i and parity π_i to a final state E_f, I_f and π_f, Figure 3.14. The energy of the γ is given by

$$E_\gamma = E_i - E_f, \tag{3.28}$$

if nuclear recoil is neglected. The emitted photon carries angular momentum $L\hbar$. This value of $L\hbar$, relating to the multipolarity of the transition, will be within limits

$$|I_i - I_f| \leqslant L \leqslant I_i + I_f. \tag{3.29}$$

The multipolarity, L, of photons can be described as transitions of *dipole* ($L = 1$), *quadrupole* ($L = 2$), *octupole* ($L = 3$), etc. Transitions in which L takes on the value $L = I_i - I_f$ are known as *stretched*, whereas others are known as *folded* transitions. The parity change in the transition is given by the selection rules

$$\pi(EL) = \pi_i\pi_f = (-1)^L \tag{3.30}$$

for an electric, E, transition of order L, and is

$$\pi(ML) = \pi_i\pi_f = (-1)^{L+1} \tag{3.31}$$

for a magnetic, M, transition. From the above equations it is clear that electric transitions will have even parity if the angular momentum carried away in the transition is even, and magnetic transitions will have even (parity) if the angular momentum transferred is odd. For example, for a transition from a state $I_i = 4^+$ to $I_f = 2^+$, the permitted values for L are 2, 3, 4, 5 and 6, with no change in parity, hence the radiation emitted is $E2$, $M3$, $E4$ $M5$ and $E6$. For a transition from a state $I_i = 5^-$ to $I_f = 4^+$, the permitted values for L are 1, 2, 3, 4, 5, 6, 7, 8 and 9 with change in parity, hence the radiation emitted is $E1$, $M2$, $E3$, $M4$, $E5$, $M6$, $E7$, $M8$, and $E9$. Note that transition between two 0^+ or 0^- states, i.e. pure $L = 0$, are forbidden to proceed via a γ decay since photons (as they are Bosons) have an intrinsic spin $1\hbar$. Such transitions can occur via internal conversion or internal pair production (if $E_\gamma > 1.022$ MeV).

Table 3.1: A summary of selection rules for gamma-ray emission.

L	Multipolarity	Transition type	Parity change
1	Dipole	Electric dipole(E1)	Yes
		Magnetic dipole(M1)	No
2	Quadrupole	Electric quadrupole(E2)	No
		Magnetic quadrupole(M2)	Yes
3	Octupole	Electric octupole(E3)	Yes
		Magnetic octupole(M3)	No
L	2^L-pole	Electric 2^L-pole	No for L even
			Yes for L odd
		Magnetic 2^L-pole	Yes for L even
			No for L odd

3.6.2 Internal Conversion

A competing process to γ-ray emission is that of internal conversion. In this process, the excitation energy of the nucleus is transferred to one of the atomic electrons, causing it to be emitted from the atom. The kinetic energy of the emitted electron depends upon the electron binding energy, and the transition energy, E_γ of the γ-ray

$$T_e = E_\gamma - B_e. \qquad (3.32)$$

Electrons in different atomic orbitals have different binding energies, thus it is possible that for a given transition there are several possible electron energies. From equation 3.32, it is clear that if the transition energy is smaller than the electron binding energy for a particular shell, then the electrons in that shell cannot be emitted. The internal conversion process has a threshold energy which must be equal to electron binding energy in a particular shell. Conversion electrons are thus labelled by the atomic shell from which they originated.

The principal atomic quantum numbers n = 1, 2 and 3 correspond to the K, L and M shells, respectively. It is also possible to resolve the shell substructure, thus conversion electrons from the L (i.e. n =2) shell can be labelled L_I, L_{II}, or L_{III}, if they originated from the $2s_{\frac{1}{2}}$, $2p_{\frac{1}{2}}$, or $2p_{\frac{3}{2}}$ atomic orbitals, respectively. Following the emission of a conversion electron in the atomic shell, the vacancy left is filled by one from a higher

shell, and the difference in energy between the two shells appears in the form of an X-ray. For example, if a vacancy is created in the K shell of an atom (i.e. the most bound or 1s orbital), then when this is filled by an electron from a higher shell, a K X-ray will be emitted. If the electron drops from the L shell, a K_α X-ray will be emitted with an energy $E(K_\alpha)$ given by

$$E(K_\alpha) = E_L - E_K. \tag{3.33}$$

Vacancies created in the outer shell caused by electrons dropping down and filling the K shell are subsequently filled by electrons from even higher levels. In this way, characteristic L, M, etc. X-rays are also emitted. The yield of X-ray photons is reduced by the *Auger effect*. The Auger effect occurs when the energy liberated by an electron filling a lower shell causes the ejection of another outer-shell electron.

This characteristic X-ray emission is often useful for the γ-ray spectroscopist when determining the atomic number Z of the nucleus from which γ-rays under investigation were emitted. The Internal Conversion Coefficient (ICC), α_i, of a transition is the probability of an electron from the ith electron shell competing with gamma-ray emission and is equal to

$$\alpha_i = \frac{\lambda_{e_i^-}}{\lambda_\gamma}. \tag{3.34}$$

The total decay probability is then given by

$$\lambda_t = \lambda_\gamma(1 + \alpha). \tag{3.35}$$

The internal conversion coefficient depends on the energy of the transition, the atomic number of the nucleus and the principal atomic quantum number in approximately the following way:

$$\alpha \propto \frac{Z^3}{n^3 E_\gamma^{2.5}}. \tag{3.36}$$

It is clear that the internal conversion increases strongly with Z and with l but decreases with increasing transition energy E_γ and for higher atomic shells (n > 1). Thus it can be concluded that the internal conversion is an important effect for nuclei of high atomic
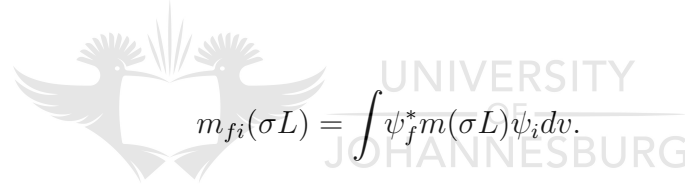
number in low-energy transitions of high multipole order l. Internal conversion coefficients are also larger for magnetic transitions than for electric transitions.

3.6.3 Transition Probabilities

For each decay that occurs, it is possible to calculate the transition probability of the radiation multipolarity. The transition per unit time (i.e. γ-emission rate) of a multipole of order L with $\sigma = E$(electric) or M(magnetic), and gamma energy E_γ is given by [14, 48, 49]:

$$\lambda(\sigma L) = \frac{P(\sigma L)}{\hbar \omega} = \frac{2(L+1)}{\epsilon_0 \hbar L[(2L+1)!!]^2} \left(\frac{\omega}{c}\right)^{2L+1} [m_{fi}(\sigma L)]^2, \qquad (3.37)$$

where ω is the rotational frequency, c-the speed of light and ϵ_0 is the dielectric constant. The expression $(2L+1)!! = (2L+1)\cdot(2L-1)...3\cdot1$. In quantum mechanics, the radiation is emitted as discrete photons and so the matrix element of the multipole operator that changes the nucleus from its initial state ψ_i to the final state ψ_f is required. It is of the form:

$$m_{fi}(\sigma L) = \int \psi_f^* m(\sigma L) \psi_i dv. \qquad (3.38)$$

This will then give a transition probability for the electric multipole of

$$\lambda(EL) \cong \frac{8\pi(L+1)}{L[(2L+1)!!]^2} \frac{e^2}{4\pi\epsilon_0 \hbar c} \left(\frac{E}{\hbar c}\right)^{2L+1} \left(\frac{3}{L+3}\right)^2 cR^{2L}, \qquad (3.39)$$

and for the magnetic multipole it will be a transition of

$$\lambda(ML) \cong \frac{8\pi(L+1)}{L[(2L+1)!!]^2} \left(\mu_p - \frac{1}{L+1}\right)^2 \left(\frac{\hbar}{m_p c}\right)^2 \left(\frac{e^2}{4\pi\epsilon_0 \hbar c}\right) \left(\frac{E}{\hbar c}\right)^{2L+1} \left(\frac{3}{L+2}\right)^2 cR^{2L-2}. \qquad (3.40)$$

Estimates of these transition probabilities can be made by using an independent particle model picture and considering transitions of a nucleon moving from one single-particle orbit to another. The estimates for decay probabilities in such cases are known as *Weisskopf single particle estimates*, Table 3.2. As they are estimates, they do not give correct theoretical values compared with the measured values.

Table 3.2: *Weisskopf single-particle estimates* for different electromagnetic multipolarities up to $L = 6$ [50, 48, 14]. Values are in s^{-1} units when E is in MeV and A is the atomic mass number.

Radiation Multipole L	Electric	Magnetic
1	$1.0 \times 10^{14} A^{2/3} E^3$	$3.1 \times 10^{13} E^3$
2	$7.3 \times 10^{7} A^{4/3} E^5$	$2.2 \times 10^{7} A^{2/3} E^5$
3	$3.4 \times 10^{1} A^{2} E^7$	$1.0 \times 10^{1} A^{4/3} E^7$
4	$1.1 \times 10^{-5} A^{8/3} E^9$	$3.3 \times 10^{-6} A^{2} E^9$
5	$2.4 \times 10^{-12} A^{10/3} E^{11}$	$7.4 \times 10^{-13} A^{8/3} E^{11}$
6	$4.0 \times 10^{-19} A^{4} E^{13}$	$1.2 \times 10^{-19} A^{10/3} E^{13}$

From these Weisskopf estimates it is possible to formulate the following two conclusions, i.e.

1. the lower multipolarities are dominant,

2. for a given order of multipole radiation, the electric radiation is more favoured than the magnetic radiation. In the medium and heavy nuclei this can be as much as two orders of magnitude.

3.7 Quasiparticle Excitations

In the Semi Empirical Mass Formula (SEMF) discussed in Section 3.2, the binding energy due to the pairing force is accounted for by the term

$$\delta(A, Z) = \left\{ \begin{array}{cl} 34.A^{-3/4} & \text{for even-even} \\ 0 & \text{for odd-even} \\ -34.A^{-3/4} & \text{for odd-odd} \end{array} \right\} \text{nuclei}, \qquad (3.41)$$

where the units of $\delta(A, Z)$ are in MeV. Clearly, such a pairing force favours even-even nuclei more than odd-N and/or odd-Z nuclei, hence making even-even nuclei more stable.

The probability amplitudes for the ith orbital being occupied and unoccupied by a pair of

particles are v_i and u_i respectively, such that

$$v_i{}^2 + u_i{}^2 = 1. \tag{3.42}$$

For a nucleus in its ground state, pairs of nucleons occupying orbitals close to the unoccupied levels (i.e. at the Fermi surface), can scatter to the "empty" single-particle states. When a particle is excited to an orbital with a partial occupation probability, nucleon pairs can no longer scatter into the orbital. This is due to the Pauli principle and the probability of occupation for a nucleon pair diminishes. This phenomenon is referred to as blocking. The state at the new energy is called a *single-quasiparticle* state. It is formed by the breaking nucleon pairs and occupying excited single-nucleon orbitals. Its energy is given by [37]

$$E_i = \sqrt{(\varepsilon_i - \lambda)^2 + \Delta^2}, \tag{3.43}$$

where ε_i is the single-particle energy of the state i and λ is the Fermi energy lying in the region between the occupied and unoccupied levels. Δ is the pair gap parameter expressed by

$$\Delta = G \sum_{i \neq i_j} u_i v_i, \tag{3.44}$$

where G is the monopole pairing strength and i_j represents the indices of the single occupied orbitals. From the definition of v_i^2 in Equation 3.42, the total number of particles is [55]

$$n = 2 \sum_i v_i^2, \tag{3.45}$$

and the probability of a state being occupied is given by

$$v_i^2 = \frac{1}{2} \left[1 - \frac{(\varepsilon_i - \lambda)}{E_i} \right]. \tag{3.46}$$

These two equations 3.45 and 3.46 define the Fermi surface λ.

3.8   Isomerism

Atomic nuclei, like all quantum systems, when excited, will eventually decay to the lowest energy configuration. A nuclear isomer can be defined as an excited, metastable state of atomic nuclei whose decay is generally suppressed, most often due to nuclear structure effects, leading to an excited system with an uncharacteristically long lifetime [51, 52]. The typical half-life, $t_{1/2}$ of an excited nuclear state is of the order of $10^{-12}(pico)$ seconds,

however half-lives of isomeric states are prolonged ranging from 10^{-9} seconds to greater than 10^{15} years. Isomers can de-excite by any of the following mechanisms: α, β, γ-ray emission, or internal conversion. The most prevalent form of radioactive decay mode is γ-decay.

The prolonged lifetime of isomeric states is generally due to the fact that the electromagnetic decay of the excited state requires a significant change in shape, spin, and/or spin orientation. This combined with low transition energy lead to long mean-life for the nuclear state. Depending upon the mechanism that inhibits their decay, nuclear isomers can be categorized into three different forms, which are *shape* isomers, *spin* traps and K-traps.

Shape Isomers

The shape isomers arise when there is a second energy minimum of the nuclear potential surface. This second minimum has a different deformation to that of the ground-state minimum and therefore there is potential barrier between the two. Decay to the ground state by electromagnetic decay can compete with fission. Fission into two or more lighter nuclides, the so called "fission" isomers.
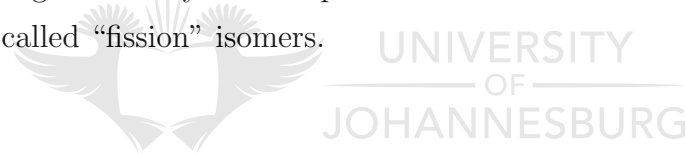
Spin Isomers

Spin trap isomers occur because of the difficulty to satisfy spin selection rules which basically need conservation angular momentum, from Section 3.6.1. If an excited state is created at high spin and low excitation energy, and the only states available for it to decay have much lower angular momentum. When such a nuclear state decays via an electromagnetic transition, the amount of angular momentum removed from the system would have a high multipolarity L, equivalent to the angular momentum carried by the radiation. Such transitions characterised by a large change in spin required in a decay, tend to have smaller probability and as such longer half-life. This work mainly focusses on the K-isomers as the nucleus of interest ^{178}Hf is characterized by this type of isomerism.
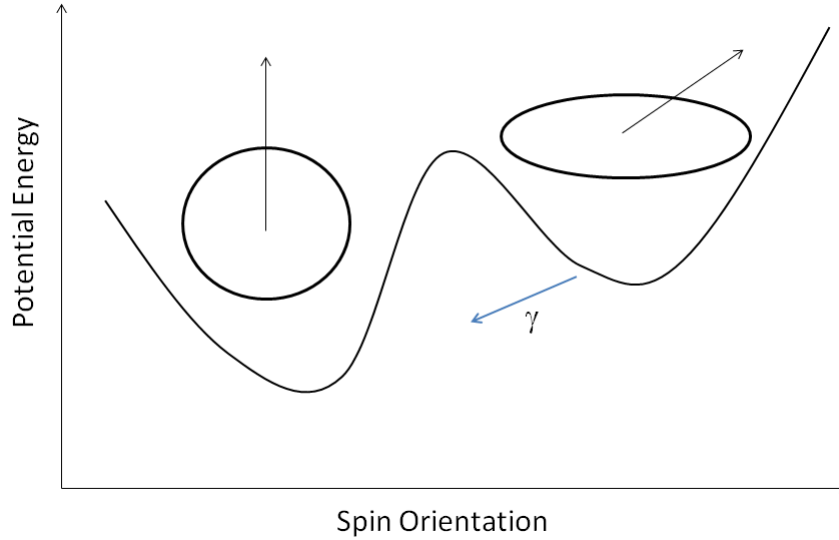
Figure 3.15: The projection of the spin on the nuclear deformation axis.

3.8.1 K-isomers

K-isomerism (i.e. K-trap) is found only in axially symmetric, deformed prolate nuclei when there is a secondary minimum in the potential energy surface for a certain value of K, Figure 3.15. These nuclei are found away from the closed shells. Such K-traps involve transitions with large changes in the orientation of the angular momentum. The selection rule for an allowed electromagnetic decay with multipolarity λ, between initial and final states of K_i and K_f respectively is given by:

$$|K_i - K_f| = \Delta K \leq \lambda. \tag{3.47}$$

Any transition with $\Delta K > \lambda$ violates this selection rule and as such is hindered. Such a transition is called a "K-*forbidden*" transition, and the isomer formed is called a "K-trap" [53]. The *degree of forbiddenness*, for a K-forbidden transition, ν, is given by the following equation:

$$\nu = \Delta K - \lambda. \tag{3.48}$$

For each unit of K change that exceeds the transition's multipolarity, λ, the transition rate may be reduced or hindered by a factor of about 100. The hindrance per degree of K-forbiddenness is defined by equation

$$f_\nu = \left[\frac{T_{1/2}^\gamma}{T_{1/2}^W} \right]^{\frac{1}{\nu}}, \tag{3.49}$$

where $T_{1/2}^{\gamma}$ is the partial γ-ray half life and $T_{1/2}^{W}$ is the Weisskopf single-particle estimate for the given half-life.

For example, in ^{178}Hf one of the most famous isomers, $I = 16^{+}$ at 2.447 MeV has a half-life of 31 years. This long lived four quasi-particle $K^{\pi} = 16^{+}$ state is constructed by coupling of $\nu^{2}, 8^{-}$ and $\pi^{2}, 8^{-}$ components, with the configuration: $\nu^{2}\{\frac{7}{2}^{-}[514], \frac{9}{2}^{+}[624]\} \otimes \pi^{2}\{\frac{7}{2}^{+}[404], \frac{9}{2}^{-}[514]\}$. The decay of this $I = 16^{+}$ state is highly suppressed not only because a change of K by at least 8 units is necessary, but also because the transition has to carry a high multipolarity λ, due to large angular momentum differences between the initial ($J = 16^{+}$) and energetically feasible final states, $J = 11^{-}$ and 12^{-} members of the $K^{\pi} = 8^{-}$ band. However, the $\Delta K = 8$ decays, do take place. One reason for the observation of such "forbidden" transitions can be attributed to Coriolis mixing, that can occur between states with the same spin, but different K values. For instance, when the levels of two bands lie close in energy low-K and high-K components can mix into initial and final states respectively, thus reducing ΔK, resulting in faster transition.

Chapter 4

RESULTS AND DATA ANALYSIS

The time-correlated particle-γ-γ coincidence data were sorted offline into particle-gated E_γ-E_γ matrices. All events within 856 *ns* of a detected particle were recorded. The analysis focused on the forward proton and triton-gated matrices. Coincidence intensities for known bands in Hafnium-178 were obtained from the two matrices. The (Proton/triton)$_\text{Forward}$ γ-γ intensity ratios were generated and plotted as function of spin, Figure 4.6, for each of the various bands Ground State Band (GSB) $K^\pi = 0^+$, $K^\pi = 8^-$, $K^\pi = 14^-$ and $K^\pi = 16^+$ bands of the ^{178}Hf isotope.

A typical Particle Identification (PID) spectrum presented in Figure 4.1 from the DIAMANT detector generated from custom-built VXI electronics [26] clearly shows the separation of *protons, deuterons, tritons* and *alpha* particles. The separate curves when gated on, allowed the selection of gamma-ray coincidences detected with AFRODITE when respective complementary ^{6}He, ^{4}He (α) and triton fragments fused with the target. "Banana" gates were set up on each region of the particle of interest. The focus of the present study is the ^{4}He and ^{6}He transfer channels which means that "banana" gates were set around triton and proton particles respectively. The γ-ray spectrum obtained in coincidence with the proton/triton particles is shown in Figure 4.2. A cascade of γ transitions depopulating the levels in the yrast rotational band of ^{178}Hf are clearly visible.

The main analysis was carried out with two matrices; one matrix proton-gated and the other triton-gated, both at forward focussed angles covering minimum angles up to a maximum of $\sim60°$ with respect to the beam axis. These symmetrized matrices contained $\sim3.7 \times 10^6$ counts in the proton gated and $\sim6.5 \times 10^6$ counts in the triton gated matrix. Coincidence intensities for GSB, $K^\pi = 8^-$, $K^\pi = 14^-$ and $K^\pi = 16^+$ bands were extracted
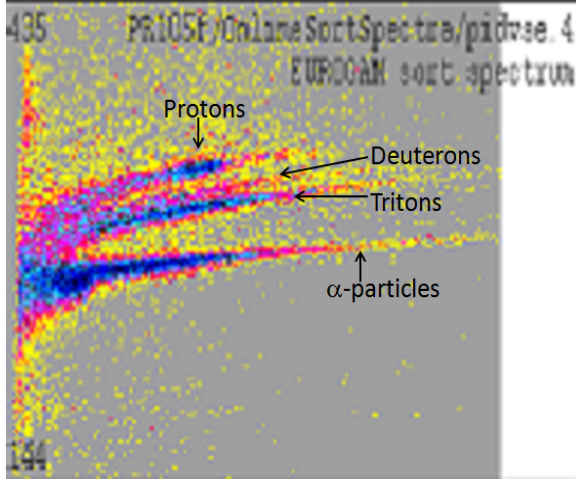
(a) Particles detected
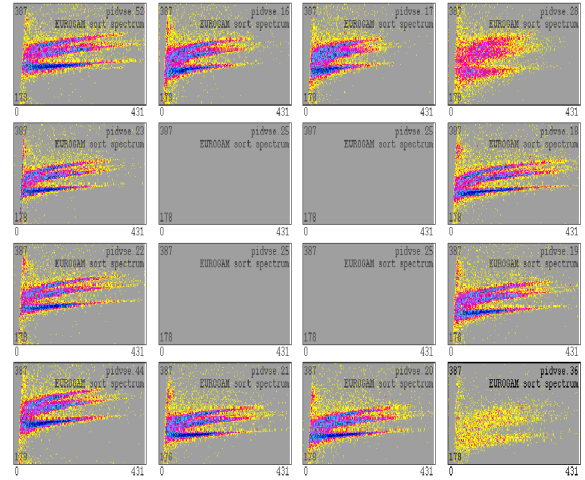
(b) Rear-section of front quadrangles
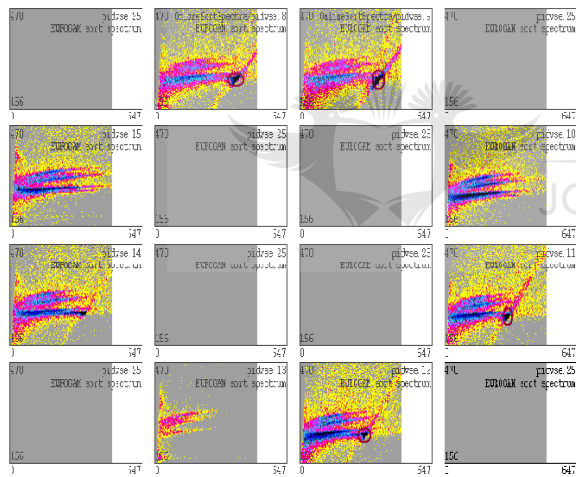
(c) Forward-section of front quadrangles
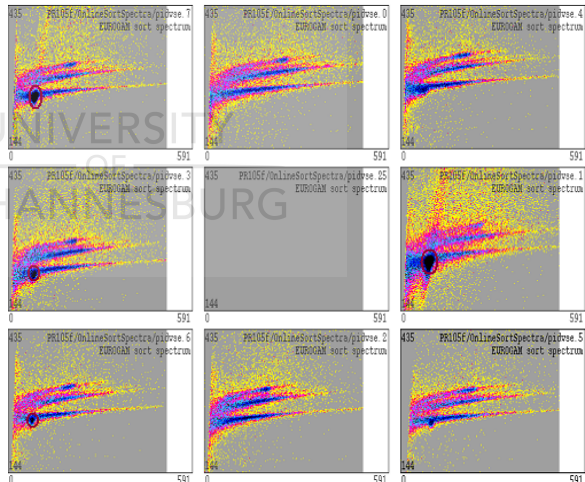
(d) Forward wall

Figure 4.1: The DIAMANT "Mini-chessboard", PID vs Energy spectra for the ^{7}Li + ^{176}Yb reaction at 50 MeV. Areas encircled in red in (c) and (d), show points of direct detector hit by the beam.

from the two matrices. The gamma-ray transition energies and intensities for these bands are listed in Table 4.1. The level scheme for ^{178}Hf extracted from the spectrum, Figure 4.2 is given in Figure 4.3 [3]. There are no new transitions or isomeric states established in ^{178}Hf isotope in this work. The γ-rays from the ground-state band in ^{178}Hf are clearly visible from the full-projection spectrum Figure 4.2. This is the strongest channel populated, formed primarily from the capture of a "^{6}He" fragment by the target followed by evaporation of four neutrons. The ground state band members are observed clearly up to the $16^+ \longrightarrow 14^+$ transition. The triton-gated matrix for the "^{4}He" captured fragment also shows ^{178}Hf isotope strongly populated.

Figure 4.4, is a spectrum of ^{180}Hf populated through the reaction channel (^{6}He, 2n) in the proton tagged matrix. This confirms the breakup of the ^{7}Li beam into "^{6}He" and "p" with relative high Q-values $\sim$9.9 MeV compared to the ^{7}Li $\longrightarrow ^4$He $+ ^3$H channel with Q = 2.5 MeV, from Equation 2.3.

4.1 Ground State Band:

Figure 4.5 compares proton with triton tagged matrices, for the spectra generated by summing gates on 93 keV and 214 keV γ-rays which occur coincidentally as cascade transitions in the strongly populated ground state band in ^{178}Hf. All the strong peaks in the spectra are accounted for in the level scheme.

The ratios of the γ-γ coincidence intensities of the form (Proton/Triton)$_{\texttt{Forward}}$ for each peak in the ground state band were generated. These ratios are plotted as a function of spin for each of the bands populated Figure 4.6. The GSB shows no change in the proton-triton intensity ratio with increase in spin.

4.2 The $K^\pi = 8^-$ Band:

The spectra showing the 8^- band is given in Figure 4.7. This band is built on $K^\pi = 8^-$ isomer at 1.149 MeV, with a half-life of 4 s. It is a 2 quasi-particle state formed from the $\nu^2\{\frac{7}{2}^-[514] \otimes \frac{9}{2}^+[624]\}$ particle configuration. This band has been populated up to spin 15 $\hbar$.

The proton-triton intensity ratios for the 8^- band members show no dependence on spin,
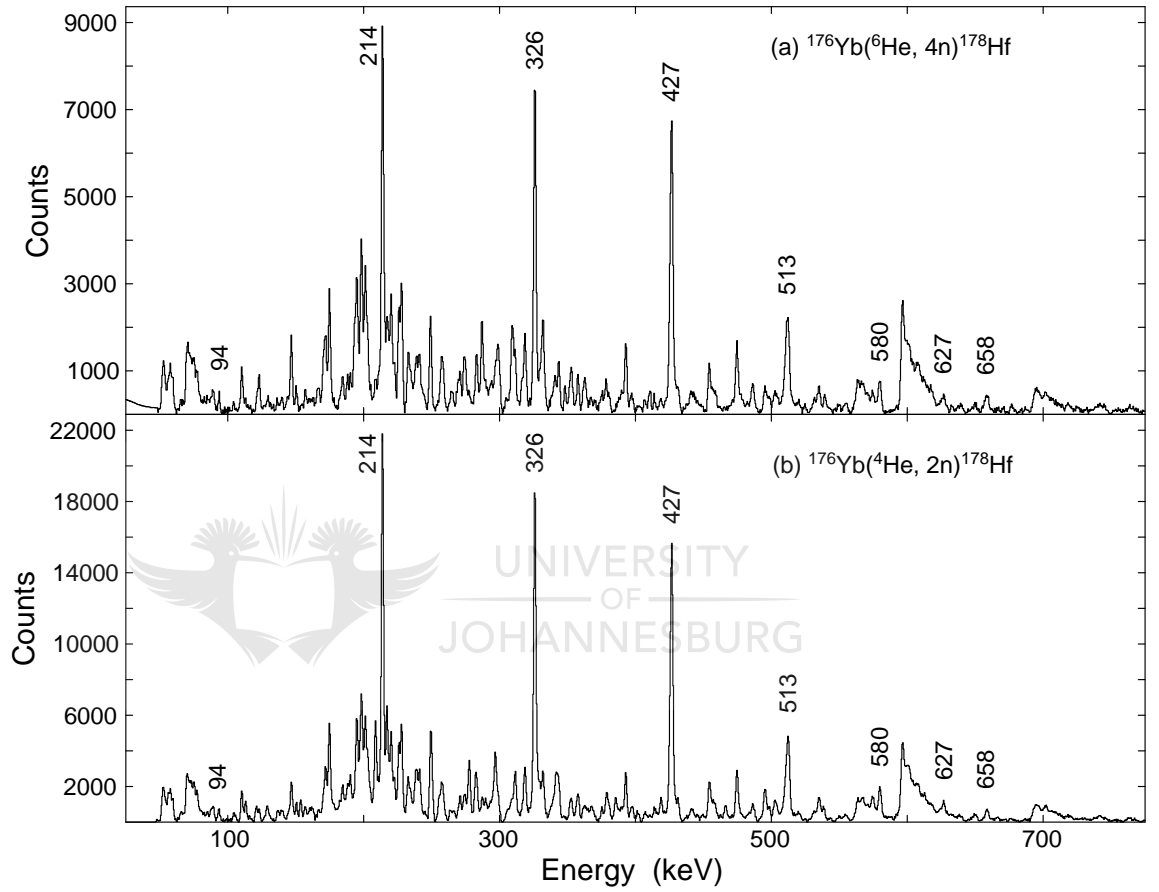
Figure 4.2: Total projection spectra of the ^{7}Li + ^{176}Yb reaction from a 2-dimensional symmetric $\gamma-\gamma$ matrix, with (a) proton tagged spectrum and (b) triton tagged spectrum.
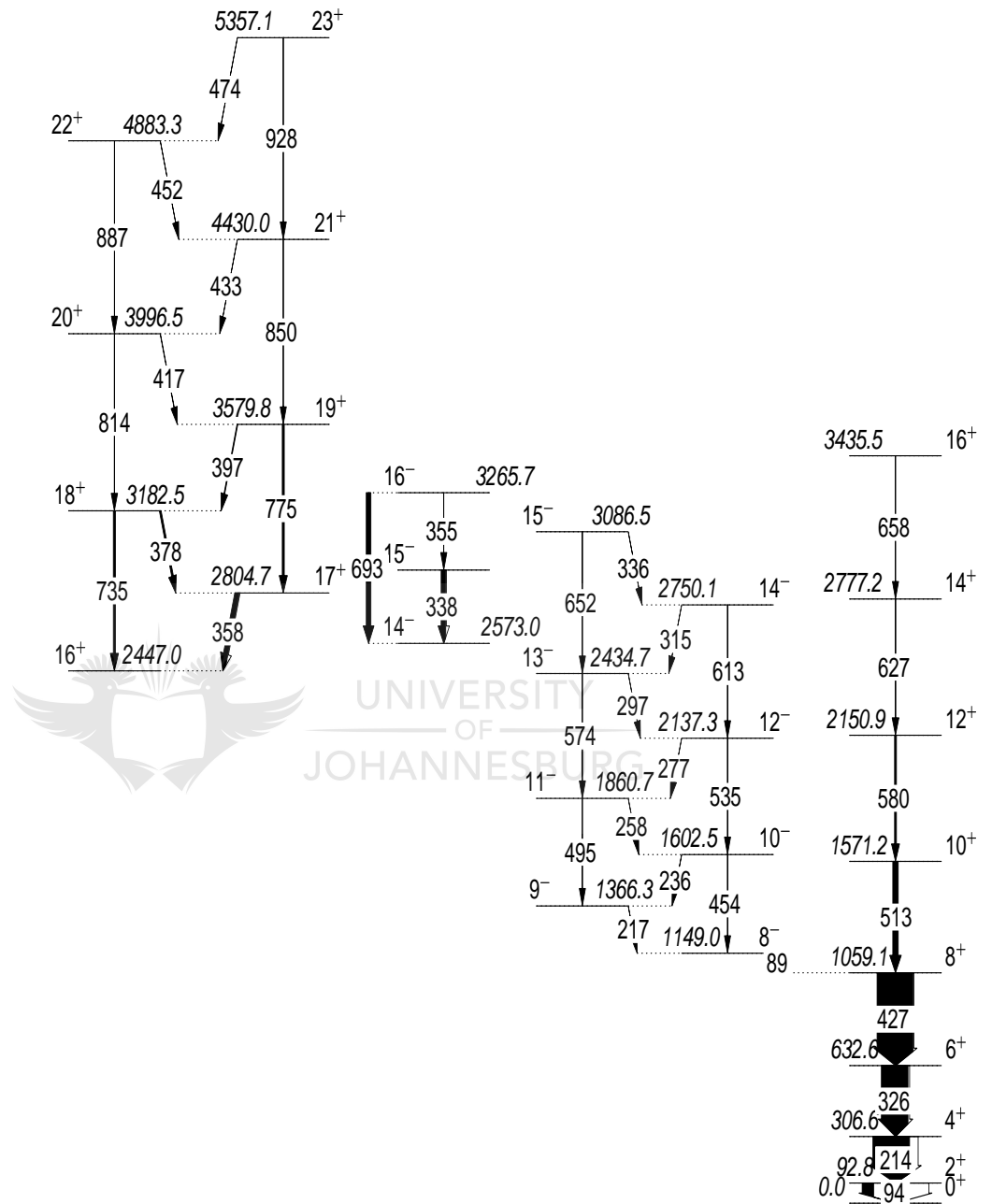
Figure 4.3: A level scheme of ^{178}Hf [3] extracted from the spectrum in Figure 4.2, produced through ^{176}Yb(^{4}He, 2n)^{178}Hf exit channel of this experiment.
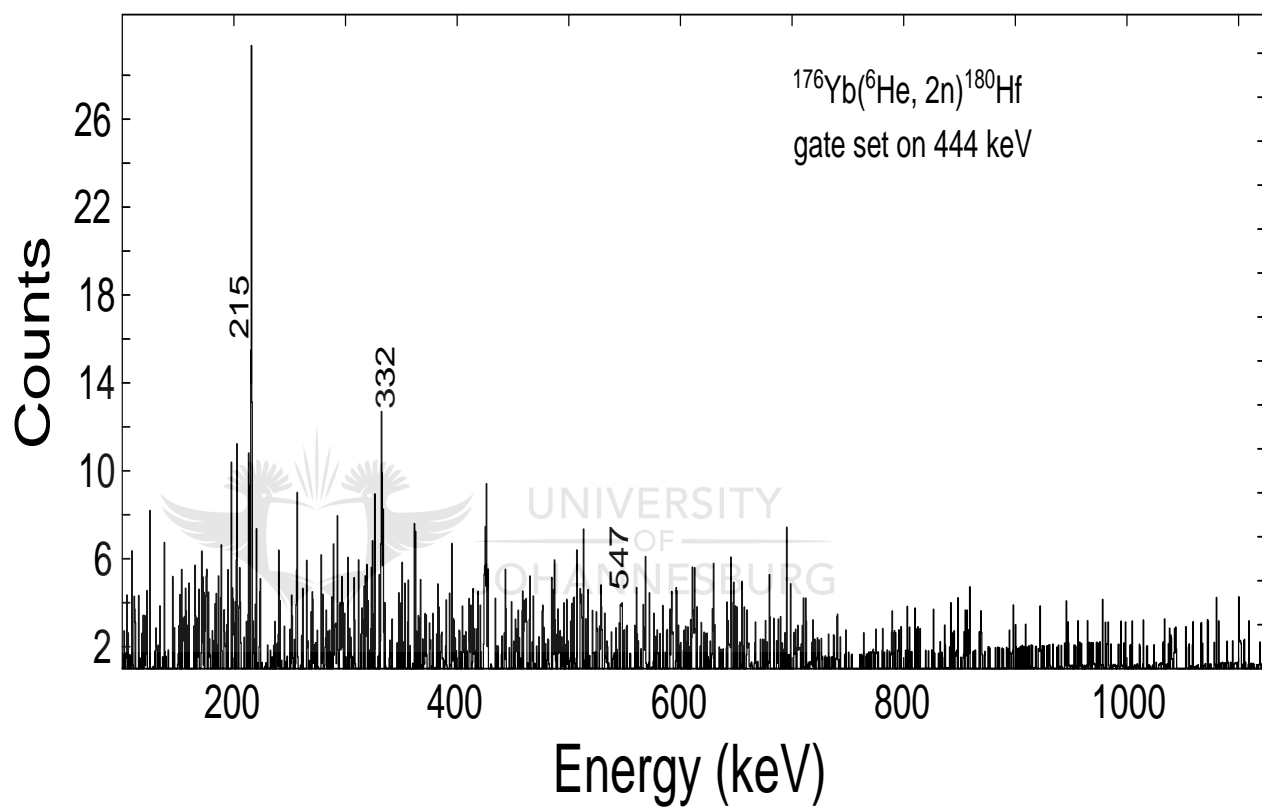
Figure 4.4: ^{180}Hf spectra showing the ground-state band members for the proton tagged spectrum produced through ^{176}Yb(^{6}He, 2n)^{180}Hf exit channel of this experiment.
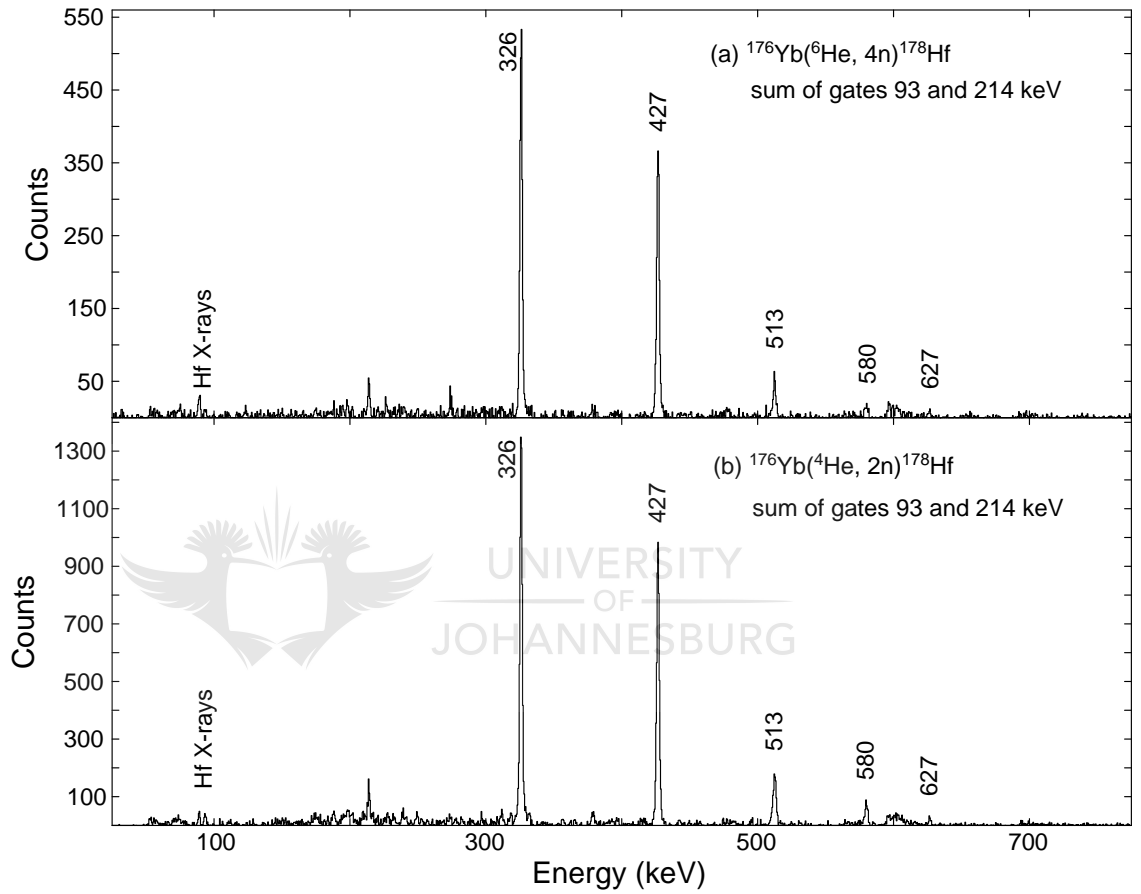
Figure 4.5: Coincidence spectra generated by summing gates set on 93 keV and 214 keV of the ground-state band, with (a) proton tagged spectrum and (b) triton tagged spectrum.
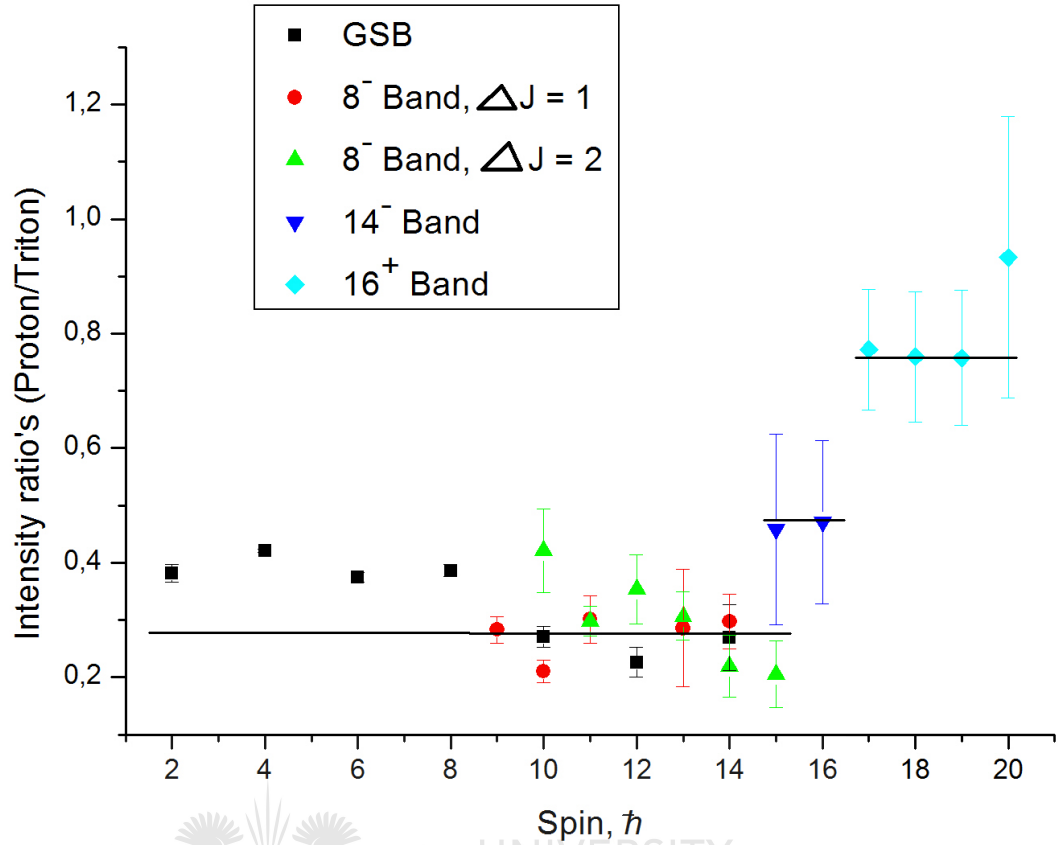
Figure 4.6: Intensity ratios of the proton-gated to triton-gated γ-ray yields as a function of spin for $K^\pi = 0^+$ (Ground-State Band), $K^\pi = 8^-$, $K^\pi = 14^-$ and $K^\pi = 16^+$ bands in ^{178}Hf. The lines are drawn to guide the eye.

Figure 4.6.

4.3 The $K^\pi = 14^-$ Band:

This band is built on the $K^\pi = 14^-$ isomer, formed by combining either the ν^2, 8^- component with the 6^+, $\pi^2\{\frac{5}{2}^+[402] \otimes \frac{7}{2}^+[404]\}$ state, or the π^2, 8^- component with the 6^+ state from the $\nu^2\{\frac{5}{2}^-[512] \otimes \frac{7}{2}^-[514]\}$ configuration.

The yield ratios for the members of this band, $K^\pi = 14^-$ are comparatively higher than those of the GSB and 8^- band. The proton-triton intensity ratios show no change with increase in spin as illustrated in Figure 4.6.

67
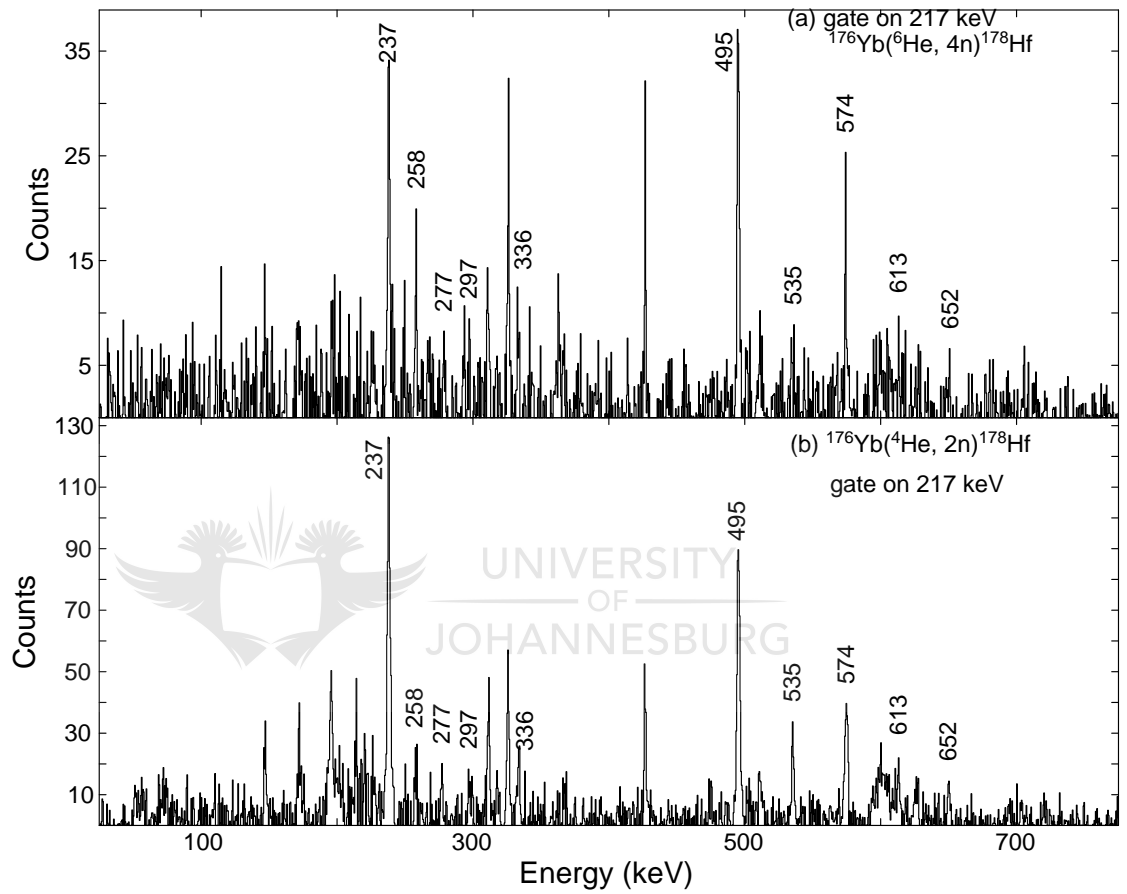
Figure 4.7: Coincidence spectra generated by setting a gate on 217 keV γ-ray of the 8^- band, with (a) proton tagged spectrum and (b) triton tagged spectrum.

4.4 The $K^{\pi} = 16^+$ band:
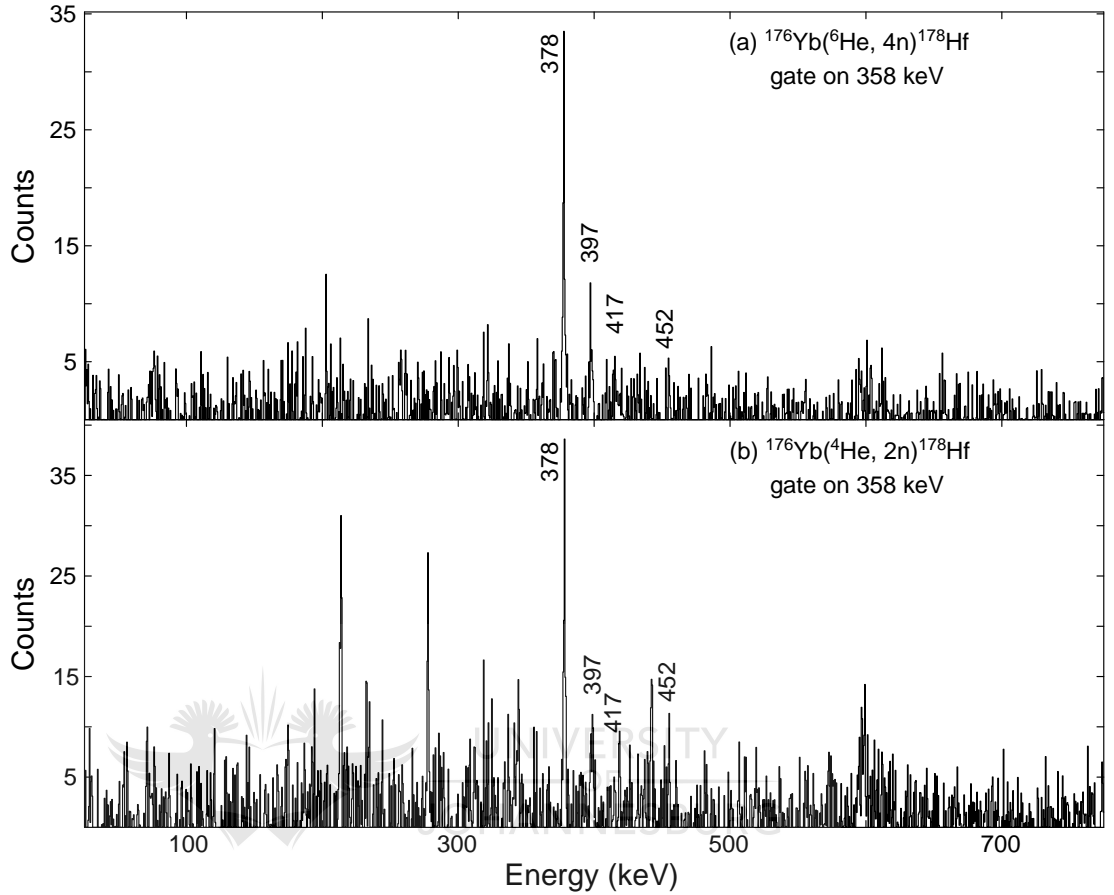
Figure 4.8: Coincidence spectra generated by setting a gate on 358 keV γ-ray of the 16^+ band, with (a) proton tagged spectrum and (b) triton tagged spectrum.

Figure 4.8 is showing a spectra of the 16^+ band . This band is built on $K^{\pi} = 16^+$ isomer. This isomer is based on coupling $\nu^2_{8^-} \otimes \pi^2_{8^-}$ configurations as explained in detail in Section 3.8.1. The ratios of the γ-γ coincidence intensities were also generated for the 16^+ band, as represented in Figure 4.6. The yield ratios for the 16^+ band also show no change in ratio with increase in spin, however they are comparatively higher than those of the GSB, 8^- and 14^- bands.

The rise in the (proton/triton) intensity ratio at higher spins can be attributed to the differences in mass of the fused fragments, with ^{6}He being 50% more massive than ^{4}He.

69

The average angular momentum transferred to the target nucleus in the capture of projectile fragment increases linearly with captured mass. The less mass-asymmetric the beam/target combination for a given compound nucleus, the higher the maximum angular momentum that can be induced into the system.

Table 4.1: Intensities of counts (given as total counts) extracted from proton and triton-γ-γ matrices, for channels populating ^{178}Hf.

E_γ	J^π	I_γ-proton-gated	I_γ-triton-gated	Intensity ratios(p/t)
Ground State Band:				
*94	2^+	898	2352	0.381(15)
*214	4^+	31156	74007	0.421(3)
326	6^+	2412	6436	0.375(9)
427	8^+	1876	4857	0.386(1)
513	10^+	282	1040	0.271(18)
580	12^+	96	424	0.226(26)
627	14^+	28	104	0.269(57)
8^- Band:				
217	9^-	194	685	0.283(23)
236	10^-	143	679	0.211(19)
258	11^-	69	229	0.301(41)
†277	12^-	0	68	0
297	13^-	10	35	0.286(102)
315	14^-	50	168	0.298(48)
454	10^-	48	114	0.421(72)
495	11^-	164	550	0.298(27)
535	12^-	46	130	0.354(61)
574	13^-	69	225	0.307(42)
613	14^-	20	91	0.220(54)
650	15^-	15	73	0.205(58)
14^- Band:				
337	15^-	11	24	0.458(166)
355	16^-	16	34	0.471(143)
16^+ Band:				
358	17^+	95	123	0.772(105)
378	18^+	79	104	0.760(113)
397	19^+	72	95	0.758(118)
417	20^+	28	30	0.933(245)

* The intensities of gamma-ray were taken from fullprojection matrix.

† Omitted from the plot.

Chapter 5

SUMMARY AND CONCLUSION

This work is the result of the analysis of an experiment which was proposed to expand our knowledge of incomplete fusion reaction. The experimental signatures of incomplete fusion reactions are the observation of strongly forward-peaked charged particles, with a ^{7}Li beam; protons, deuterons, tritons and alphas as shown in Figure 4.1 with much higher energies than observed in conventional fusion-evaporation reactions. These charged particles have been used for a very efficient channel selection.

It has been possible to extract the level scheme exclusive to a particular channel for the production of the ^{178}Hf, as shown in Figure 4.3. The relative cross-section for various reaction channels could therefore be extracted. Gamma intensities for proton and triton gated spectra were extracted for the different bands; the Ground State Band, 8^-, 14^- and 16^+ of the ^{178}Hf isotope. The yield ratios (proton to triton) for the gamma intensities at forward angles for each band were determined. These have been plotted as function of angular momentum of the residual nucleus, as shown in Figure 4.6. From the plot, all bands (GSB, 8^-, 14^- & 16^+) show no change in the proton-triton intensity ratio with increase in spin, i.e. the yield ratios are spin independent. However, there are observable differences when bands are compared. The GSB and 8^- bands show relatively low yield ratios compared to 14^- and 16^+ bands. The 16^+ band has a further higher yield ratio compared to the 14^- band. At high spins, Ytterbium-176 show a relatively high cross-section for incomplete fusion with Helium-6 as compared to Helium-4 (the alpha particle). The captured Helium-6 particle, being 50% more massive than Helium-4 would induce higher maximum angular momentum into the system than the latter particle (^{4}He). This work has therefore produced data which gives insight to the reaction mechanisms for

incomplete fusion processes.

In concluding, it should be noted that there remain several interesting experiments, some of which complement the work presented here and some of a more general nature should be considered. A study of ^{7}Li breakup at forward angles and middle/backward angles for heavy targets would clearly be interesting. A comparison between the ^{7}Li, ^{9}Be induced reactions and the unstudied, but definitely feasible reactions, would yield helpful spectroscopic insights.

References

[1] G. D. Dracoulis, A. P. Byrne, T. Kibedi, T. R. McGoram, and S. M. Mullins, "Incomplete fusion as a spectroscopic tool," *J. Phys. G: Nucl. Part. Phys.*, vol. 23, pp. 1191–1202, 1997.

[2] K. E. G. Lobner, "Systematics of Absolute Transition Probabilities of K-forbidden gamma-ray transitions," *Physics Letter B*, vol. 26, pp. 369–370, 1968.

[3] S. M. Mullins, G. D. Dracoulis, A. P. Byrne, T. R. McGoram, S. Bayer, W. A. Seale, and F. G. Kondev, "Rotational band on the 31 yr 16^+ isomer in ^{178}Hf," *Physics Letters B*, vol. 393, pp. 279–284, 1997.

[4] S. M. Mullins, A. P. Byrne, G. D. Dracoulis, T. R. McGoram, and W. A. Seale, "High-spin and rotational states in the stable nucleus ^{177}Hf: Evidence for reaction-dependent spin population," *Physical Review C*, vol. 58, pp. 831–845, 1998.

[5] T. Fukuda, T. Shimoda, T. Inamura, and M. Ishihara, "Gamma-rays from an incomplete fusion reaction induced by 95 MeV ^{14}N," *Physics Letter B*, vol. 16, pp. 51–54, 1977.

[6] D. R. Zolnowski, H. Yamada, S. E. Cala, A. C. Kahler, and T. T. Sugihara, "Evidence for "Massive Transfer" in Heavy-Ion Reactions on Rare-Earth Targets," *Physical Review Letters*, vol. 41, no. 2, pp. 92–95, 1978.

[7] J. Wilczyński, K. Siwek-Wilczyńska, J. van Driel, S. Gonggrip, D. C. J. M. Hageman, R. V. F. Janssens, J. Lukasiak, R. H. Siemssen, and S. Y. van der Werf, "Binary *l*-matched reactions in ^{14}N + ^{159}Tb collisions," *Nuclear Physics A*, vol. 373, pp. 109–140, 1982.

[8] A. Mukherjee and M. K. Pradhan, "Influence of Projectile Breakup on Complete Fusion," *PRAMANA-journal of physics*, vol. 75, pp. 99–107, 2010.

[9] H. Ejiri and M. J. A. de Voigt, *Gamma - Ray and Electron Spectroscopy in Nuclear Physics.* Oxford University Press, 1989.

[10] R. Bass, "Fusion of Heavy Nuclei in a Classic Model," *Nuclear Physics **A***, vol. 231, pp. 45–63, 1974.

[11] P. Regan, "Post Graduate Nuclear Experimental Techniques (4NET) Course Notes." 1, oct 2003.

[12] M. J. A. de Voigt, J. Dudek, and Z. Szymanski, "High-spin phenomena in atomic nuclei," *Reviews of Modern Physics*, vol. 55, no. 4, pp. 949–1046, 1983.

[13] R. Bass, *Nuclear Reactions with Heavy Ions.* Springer-Verlag, New York, 1980.

[14] K. S. Krane, *Introductory Nuclear Physics.* John Wiley & Sons, 1988.

[15] D. A. Bromley, *Treatise on Heavy-Ion Science.* Plenum Press New York, 1984.

[16] Z. Szymanski, *Fast Nuclear Rotation.* Oxford University Press, 1983.

[17] H. Cember, *Introduction to Health Physicis.* 3rd, McGraw-Hill, 3rd ed., 1996.

[18] W. R. Leo, *Techniques for Nuclear and Particle Physics Experiments: A How - to Approach.* Springer - Verlag, 1987.

[19] G. F. Knoll, *Radiation Detection and Measurement.* John Wiley & Sons, 3rd ed., 2000.

[20] P. M. Jones, L. Wei, F. A. Beck, P. A. Butler, T. Byrski, G. Duchene, G. de France, F. Hannachi, G. D. Jones, and B. Kharraja, "Calibration of the new composite "clover" detector as a compton polarimeter for the EUROGAM array," *Nuclear Intsruments and Methods in Physics Research **A***, vol. 362, pp. 556–560, 1995.

[21] R. T. Newman, J. J. Lawrie, B. R. S. Babu, M. S. Fetea, S. V. Fortsch, J. V. Nangaleswaran, D. A. Raave, C. Rigollet, J. F. Sharp-Schafer, C. J. Stevens, F. D. Smith, G. F. Steyn, C. V. Wikner, D. G. Aschman, R. Beetge, R. W. Fearick, G. K. Mabala, S. Murray, D. G. Roux, W. Whittaker, and N. J. Ncapayi, "Proceedings of Balkan School on Nuclear Physics," *Balkan Physics Letter*, 1998.

[22] K. A. Korir, *Mechanisms of Heavy Ion Reactions and De-excitation in Processes Initiated by Projectiles at Intermediate Energies.* PhD thesis, University of Witwatersrand, 2006.

[23] G. Duchene, F. A. Beck, P. J. Twin, D. Curien, L. Han, C. W. Beausang, M. A. Bently, P. J. Nolan, J. Simpson, and G. de France, "The Clover: a new generation of composite Ge detectors," *Nuclear Instruments and Methods in Physics Research* **A**, vol. 1, no. 432, pp. 90–110, 1999.

[24] W. H. Trzaska, "Recommended data on selected gamma-ray and conversion-electron calibration sources," *Nuclear Intsruments and Methods in Physics Research* **A**, vol. 297, pp. 223–229, 1990.

[25] J. Scheurer, M. Aiche, M. Aleonard, G. Bourgine, D. Boivin, D. Cabaussel, J. Chemin, T. Doan, J. Goudour, M. Harston, A. Brondi, G. L. Rana, R. Moro, E. Vardaci, and D. Curien, "Improvements in the in-beam γ-ray spectroscopy provided by an ancillary detector coupled to a Ge γ-spectrometer: the DIAMANT-EUROGAM II example," *Nuclear Instruments and Methods in Physics Research* **A**, vol. 385, pp. 501–510, 1997.

[26] J. Gál, G. Hegyesi, J. Molnár, B. Nyakó, G. Kalinka, J. Scheurer, M. Aléonard, J. Chemin, J. Pedroza, K. Juhász, and V. Pucknell, "The VXI electronics of the DIAMANT particle detector array," *Nuclear Instruments and Methods in Physics Research* **A**, vol. 516, pp. 502–510, 2004.

[27] J. Cresswell and J. Sampson. http://nnst.dl.ac.uk/MIDAS/manual/MTsort/edoc033, 2006.

[28] D. C. Radford, "Background subtraction from in-beam HPGe coincidence data sets," *Nuclear Instruments and Methods in Physics Reaserch* **A**, vol. 361, pp. 306–316, 1994.

[29] D. C. Radford, "ESCL8R and LEVIT8R: Software for interactive graphical analysis of HPGe coincidence data sets," *Nuclear Instruments and Methods in Physics Research* **A**, vol. 361, pp. 297–305, 1995.

[30] A. Kramer-Flecken, T. Morek, R. M. Lieder, W. Gast, G. Hebbinghaus, H. M. Jager, and W. Urban, "Use of DCO Ratios for Spin Determination in γ-γ Coincidence Measurements," *Nuclear Instruments and Methods in Physics Research* **A**, vol. 275, pp. 333–339, 1989.

[31] K. S. Krane, R. M. Steffen, and R. M. Wheeler, "Directional Correlations of Gamma Radiations Emitted from Nuclear States Oriented by Nuclear Reactions or Cryogenic Methods," *Nuclear Data Tables*, vol. 11, no. 5, pp. 351–406, 1973.

[32] E. L. Lawrie, "Experimental Nuclear Structure notes." Notes, 2008.

[33] L. W. Fagg and S. S. Hanna, "Polarization Measurements on Nuclear Gamma Rays," *Reviews of Modern Physics*, vol. 31, no. 3, pp. 711–758, 1959.

[34] B. Povh, K. Rith, C. Scholz, and F. Zetsche, *Particles and Nuclei: An Introduction to the Physical Concepts.* Springer, 2008.

[35] O. Haxel, J. H. D. Jensen, and H. E. Suess, "On the "Magic Numbers" in Nuclear Structure," *Physical Review*, vol. 75, no. 1766, 1949.

[36] M. G. Mayer, "On Closed Shells in Nuclei," *Physical Review*, vol. 75, no. 1969, 1949.

[37] R. F. Casten, *Nuclear Structure from a Simple Perspective.* Oxford Science Publications, 2000.

[38] W. E. Burcham, *Nuclear Physics: An Introduction.* Longmans, 1963.

[39] R. Woods and D. S. Saxon, "Diffuse Surface Optical Model for Nucleon-Nuclei Scattering," *Physical Review*, vol. 95, no. 577, 1954.

[40] B. R. Mottelson and S. G. Nilsson, "Classification of the Nucleonic States in Deformed Nuclei," *Physical Review*, vol. 99, pp. 1615–1617, 1955.

[41] S. G. Nilsson, C. F. Tsang, A. Sobiczewski, Z. Szymański, S. Wycech, C. Gustafson, I. L. Lamm, P. Möller, and B. Nilsson, "On the Nuclear Structure and Stability of Heavy and Superheavy Elements," *Nuclear Physics **A***, vol. 131, pp. 1–66, 1969.

[42] B. Nilsson, "Inclusion of a P_4-Term in the Deformed Shell-Model Potential," *Nuclear Physics **A***, vol. 129, pp. 445–468, 1969.

[43] G. Andersson, S. E. Larsson, G. Leander, P. Moller, S. G. Nilsson, I. Ragnarsson, S. Aberg, R. Bengtsson, J. Dudek, B. Nerlo-Pomorska, K. Pomorski, and Z. Szymanski, "Nuclear Shell Structure at very High Angular Momentum," *Nuclear Physics **A***, vol. 268, no. 205, 1976.

[44] A. Bohr, "On the Quantization of Angular Momenta in Heavy Nuclei," *Nuclear Physics **A***, vol. 81, no. 1, 1951.

[45] F. S. Stephens, R. M. Diamond, J. R. Leigh, T. Kammuri, and K. Nakai, "Decoupled Yrast States in Odd-Mass Nuclei," *Physical Review Letters*, vol. 29, no. 7, 1972.

77

[46] C. J. Gallagher and S. A. Moszkowski, "Coupling of Angular Momenta in Odd-Odd Nuclei," *Physical Review*, vol. 3, no. 5, 1958.

[47] L. W. Nordheim, "β-Decay and the Nuclear Shell Model," *Physical Review*, vol. 78, no. 294, 1950.

[48] J. M. Blatt and V. F. Weisskopf, *Theoretical Nuclear Physics*. John Wiley & Sons, 1958.

[49] A. deShalit and H. Feshbach, *Theoretical Nuclear Physics Volume 1: Nuclear Structure*. John Wiley & Sons, 1990.

[50] V. F. Weisskopf, "Radiative Transition Probabilities in Nuclei," *Physical Review*, vol. 83, no. 1073, 1951.

[51] G. Audi, O. Bersillon, J. Blachot, and A. H. Wapstra, "NUBASE: a database of nuclear and decay properties," *Nuclear Instruments and Methods in Physics Research A*, vol. 369, pp. 511–515, 1996.

[52] P. Walker and G. Dracoulis, "Energy traps in atomic nuclei," *Nature*, vol. 399, 1999.

[53] P. M. Walker and G. D. Dracoulis, "Exotic Isomers in Deformed Atomic Nuclei," *Hyperfine Interactions*, vol. 135, pp. 83–107, 2001.

[54] R. W. Gurney and E. U. Condon, "Quantum Mechanics and Radioactive Disintegration," *Physical Review*, vol. 33, no. 2, pp. 127–140, 1929.

[55] P. Ring and P. Schuck, *The Nuclear Many-Body Problem*. Springer, 1980.